ECAL photons

The clustering algorithm for the photon reconstruction is explained in [28]. It starts with a search for local maxima among the towers in the three ECAL stacks. The segments of a projective tower which share a face in common with the local maximum are linked together into a cluster. At the end of the procedure, every segment of a tower is clustered with its neighbour of maximal energy. A cluster is then accepted as a photon candidate if its energy exceeds 350 MeV and if its barycentre is at least 2 cm away from the closest charged track extrapolation.

The energy of the photon is calculated from the energy of the four central towers. The direction of the photon is determined from the barycentre of energy deposition.

In order to distinguish fake photons [1] from photons originating from π^0 decays or other physical sources several estimators are constructed and a likelihood method is used. For every photon the following estimator is defined:

$$P_\gamma = \frac{P^{genuine}}{P^{genuine} + P^{fake}} ,$$

where P^i is the estimator under the photon hypothesis of type i given by

$$P^i = \prod_i \P_j^i(x_j) ,$$

and $\P_j^i(x_j)$ is the probability density for the photon hypothesis of type i associated to the discriminating variable x_j.

These are the discriminating variables used to distinguish between genuine and fake photons:

- fractions of energy in the first and second stacks of ECAL,
- fraction of energy outside the four central ECAL towers,
- transverse size of the photon shower,
- angular distance ($d_{\gamma\gamma}$) to the nearest photon,
- distance between the barycentre of the photon and the closest charged track (a sign is computed depending on the position of the photon shower with respect to the track bending in the $r - \phi$ projection)

[1] A fake photon is a photon produced by whatever mechanism with non–physical source.

- energy of the photon.

Reference distributions of these discriminating variables have been established from the Monte Carlo simulations for genuine and fake photons.

4.3.2 π^0 reconstruction

The energy of the π^0's from tau decays at the Z^0 peak can vary from few MeV up to about the nominal beam energy. For the whole energy range, an almost constant fraction of π^0's are reconstructed from converted photons in the tracking system. At the low energy regime, one of the photons is not detected in the ECAL for most of the π^0's because of threshold, cracks or overlap with another electromagnetic or hadronic shower. These are called π^0's from residual single photons. From 5 to about 20 GeV of energy, for most of the cases the two γ's are resolved in the electromagnetic calorimeter. The energy resolution is very good in this regime (typically $\sigma_E \approx 0.02$ GeV/c^2). At high energy the two γ's showers are very close and they can only be resolved a few times. The energy resolution deteriorates with increasing energy and is $\sigma_E \approx 0.06$ GeV/c^2 at 30 GeV/c^2.

In fig. 4.1 the fractions of resolved and unresolved π^0's and single photons as a function of the π^0 energy (from ref. [36]) are summarized. It can be seen that the fraction of resolved π^0's without converted photons remains at a relatively high level above 25 GeV. This is caused by the fact that the corresponding showers quite often have large fluctuations yielding two separate photon candidates in the clustering algorithm. This effect is not well reproduced by the Monte Carlo simulation, where this shower splitting occurs less frequently. The excess of resolved π^0's at high energy corresponds to a deficit in the unresolved π^0 fraction. However, the sum of the resolved and unresolved π^0 fraction is well described by the simulation.

The mechanism for the reconstruction of each of the π^0 types is explained at length.

π^0 with two resolved γ's

The first step of π^0 reconstruction is the pairing of all photon candidates within one hemisphere, considering all possible combinations. Only photons inside a cone of 45^o around the thrust axis are considered for the pairing. A π^o identification

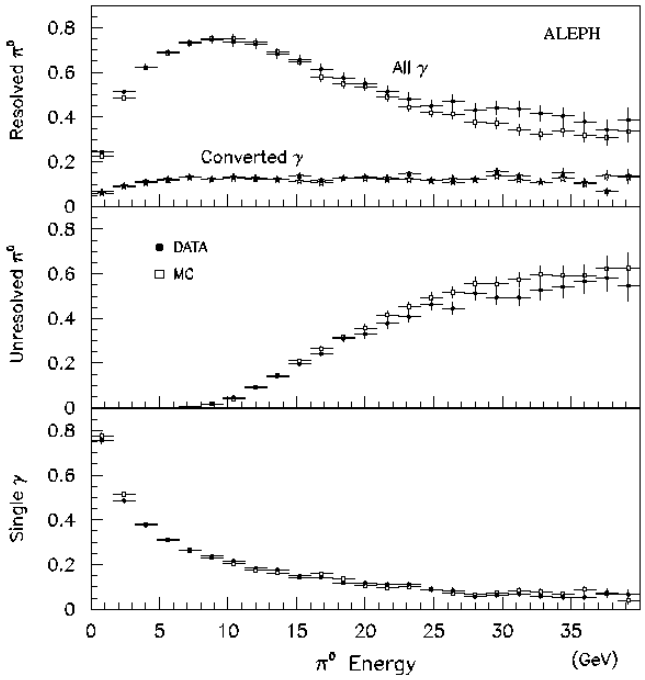

Figure 4.1: Fractions of resolved and unresolved π^0's and single photon as a function of the π^0 energy. The points represent the data, and the open squares the simulation. The proportion of π^0's containing at least one converted photon is also plotted: *Converted* γ in the first plot; again, the full points correspond to the data and the open ones to the simulation. The fraction of resolved π^0's without converted photons and that of unresolved π^0's differ for the data and the Monte Carlo simulation at a energy above 25 GeV. We comment on this effect in the text.

estimator $D^{\pi^0}_{i,j}$ for two photons i and j is defined in the following way:

$$D^{\pi^0}_{i,j} = P_{\gamma_i} \cdot P_{\gamma_j} \cdot P_{\pi^0}$$

where P_{γ_i} is the estimator for photon i to be genuine according to eq. 4.3.1 and P_{π^0} is the probability coming from a kinematic π^0–mass constrained fit.

A dependence of the π^0 invariant mass with energy is observed as explained in ref. [36]. Once the resolved π^0's are identified, a second kinematic constrained fit is performed to the nominal π^0 mass, which allows a better determination of the π^0 energy as shown in fig. 4.2 (also from ref. [36]).

π^0 with unresolved γ's

As the π^0 energy increases it becomes more difficult to resolve the two photons and the clustering algorithm may yield a single cluster. The two–dimensional energy

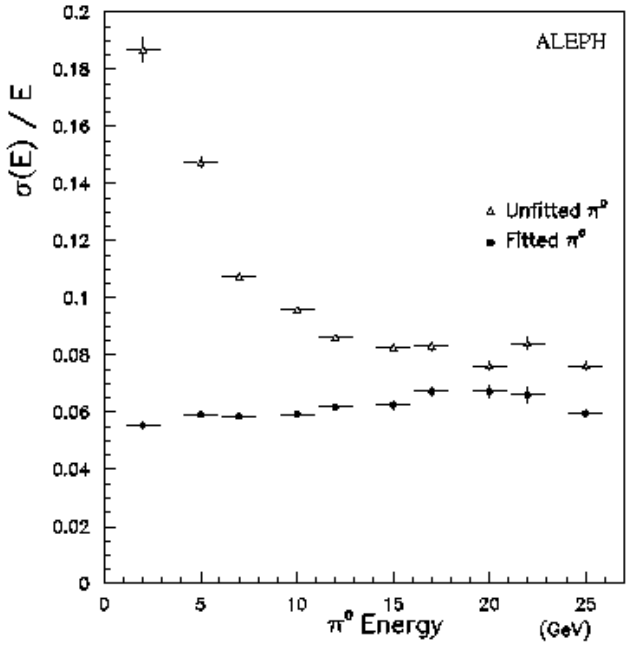

Figure 4.2: Energy resolution of the exclusive π^0's as a function of energy before and after the kinematic fit according to the simulation.

distribution in the plane transverse to the shower direction is examined and energy–weighted moments are computed. The second moment provides a measurement of the $\gamma\gamma$ invariant mass. As the photon energy increases this technique reveals a wide peak at the π^0 mass as explained in ref. [36]. We keep as π^0 candidates all single clusters not entering the previous π^0 reconstruction but having an invariant mass larger than 100 MeV/c^2 according to this method.

π^0 from residual single γ's

After the paring of photons and the cluster moment analysis, all the remaining photons inside a cone of 30^o around the thrust axis are called residual single photons. About 50% of the total are fake photons, separated from photons coming from physical processes with the estimator $P_{\gamma Res}$, explained in ref. [36]. The remaining single photons with physical origin could come from bremsstrahlung processes, radiative processes and π^0 decays. Three more estimators are calculated (P_{Brem}, P_{Rad}, $P_{\pi^0\to\gamma}$) taking into account the angle between the photon and the most energetic charged track, and the discriminating variables from section 4.3.1. Residual single

photons with $P_{\pi^0\to\gamma}$ value larger than 0.07 are declared single photons coming from π^0 decay.

4.4 Tau decay classification (TOPCLAS)

The tau decay classification is done with a code called TOPCLAS, developed for the analysis of ref. [36]. It takes into account the number of charged tracks, their identification and the number of reconstructed π^0's. A total of 13 classes are determined, but only four of them are relevant for this analysis: h, $h\pi^0$, $h2\pi^0$ and $3h$. Here h stands for either a charged kaon or a charged pion. However, we are only interested in pions and kaons are treated as background. We then name the above four classes as π, $\pi\pi^0$, $\pi 2\pi^0$ and 3π.

The invariant mass distributions for two of the classes considered are shown in fig. 4.3 (from ref. [36]). The agreement between data and the simulation is good.

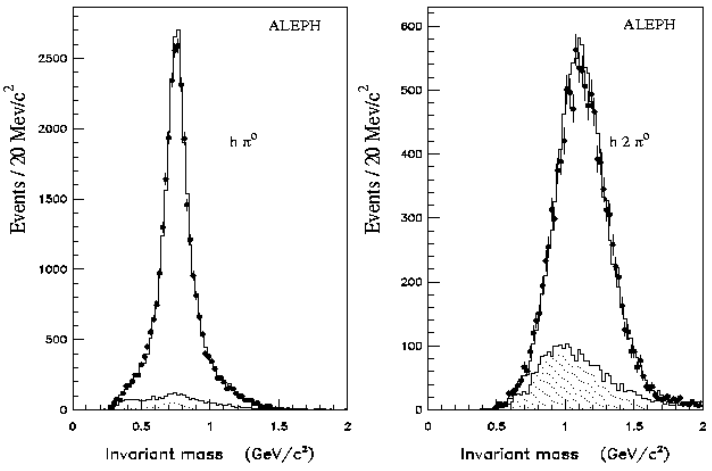

Figure 4.3: Invariant mass distributions for two of the classes of this analysis. The points with errors bars show the observed distributions, the solid histograms represent the simulated distributions and the shaded histograms account for the expected τ background.

4.5 Selection efficiencies and candidates

Four of the most sensitive observables to the weak dipole moments are spin correlations between the two taus, as it was shown in section 2.1.3. Therefore, both hemispheres need to be identified.

We have used for the event selection the tools explained before and in addition have required a correct reconstruction of the event observables (W_1, $\cos\theta_{h_1}$, ϕ_{h_1}, W_2, $\cos\theta_{h_2}$, ϕ_{h_2}), which reduces the number of candidates by 21%. The reconstruction of these event observables makes use of the tau flight direction, but this will be covered later.

Table 4.3 shows the global selection efficiencies of the decay modes considered and the percentage of τ background without requiring the correct reconstruction of the event observables. For the final analysis, we use a matrix of selection efficiencies presented in the following chapter. However, this table is useful to compare with other analysis carried out in ALEPH. The numbers of table 4.3 have been calculated with the Monte Carlo simulation and only the statistical uncertainties are given. The amount of non–tau background is not added to the table because it is completely negligible after requiring the correct reconstruction of the event observables.

We report, in table 4.4, the number of candidates in each channel as obtained from the whole data sample, in which we have required the correct reconstruction of the event observables. Finally, table 4.5 shows the data sample considered in this analysis. We present, for each of the years of data taking, the various center of mass energies and the corresponding integrated luminosities.

4.6 Monte Carlo and detector simulation

The reference Monte Carlo program in this analysis is SCOT [39], a program describing $e^+e^- \to \tau^+\tau^-$ at an energy around M_Z. It has a full description of the spin of both taus and, moreover, a complete parametrisation of the Lorentz structure of the neutral current. We have set ν_e, a_e, ν_τ, a_τ to the SM values, and have explored μ_τ and d_τ.

Nevertheless, this program does not take into account bremsstrahlung correc-

τ decay	Efficiency (%)	τ Background (%)
π–π	57.57 ± 0.39	24.18 ± 0.39
π–$\pi\pi^0$	58.39 ± 0.19	21.44 ± 0.18
π–$\pi 2\pi^0$	50.36 ± 0.31	34.09 ± 0.34
π–3π	54.29 ± 0.31	16.42 ± 0.28
$\pi\pi^0$–$\pi\pi^0$	59.76 ± 0.19	19.47 ± 0.17
$\pi\pi^0$–$\pi 2\pi^0$	52.12 ± 0.22	31.92 ± 0.23
$\pi\pi^0$–3π	54.66 ± 0.21	13.96 ± 0.19
$\pi 2\pi^0$–$\pi 2\pi^0$	45.84 ± 0.50	42.73 ± 0.56
$\pi 2\pi^0$–3π	46.98 ± 0.35	27.69 ± 0.39
3π–3π	50.98 ± 0.48	8.57 ± 0.36

Table 4.3: Selection efficiencies for the different decay channels and τ background. The errors are only due to the Monte Carlo statistic.

Class	Events	Class	Events
π–π	1901	$\pi\pi^0$–$\pi 2\pi^0$	6395
π–$\pi\pi^0$	7844	$\pi\pi^0$–$\pi 3\pi$	5242
π–$\pi 2\pi^0$	2673	$\pi 2\pi^0$–$\pi 2\pi^0$	1125
π–3π	2040	$\pi 2\pi^0$–3π	1950
$\pi\pi^0$–$\pi\pi^0$	8624	3π–3π	712
Number of all events used: 38506			

Table 4.4: Number of reconstructed events for the decay combinations.

tions, but in a first approximation we have added the initial state radiation by the simple radiator [40]

$$H(x) = \beta x^{\beta-1}(1 + \frac{3}{4}\beta + \frac{\alpha}{\pi}(\frac{\pi^2}{3} - \frac{1}{2})) - \frac{\beta}{2}(2 - x)\,, \tag{4.1}$$

where β is defined as

$$\beta = \frac{2\alpha}{\pi}(\ln\frac{s}{m_e^2} - 1), \tag{4.2}$$

and $x \in [0, 0.2]$, being the fraction of the beam energy carried by the initial state photon.

KORALZ [41] is another Monte Carlo program adequate at LEP I energies which can be used for lepton and quark pair production. This program includes initial and

1990 data		1991 data		1992 data		1993 data		1994 data		1995 data	
$\sqrt{s}$	$\mathcal{L}$	$\sqrt{s}$	$\mathcal{L}$	$\sqrt{s}$	$\mathcal{L}$	$\sqrt{s}$	$\mathcal{L}$	$\sqrt{s}$	$\mathcal{L}$	$\sqrt{s}$	$\mathcal{L}$
88.25	482	88.50	668	91.25	20999	89.50	8065	91.25	49089	89.25	8295
89.25	520	89.50	797	-	-	91.25	14434	-	-	91.25	17159
90.25	447	90.25	753	-	-	93.00	8693	-	-	91.75	72
91.25	3624	91.25	7546	-	-	-	-	-	-	93.00	9355
92.25	555	92.00	693	-	-	-	-	-	-	-	-
93.25	597	93.00	677	-	-	-	-	-	-	-	-
94.25	642	93.75	797	-	-	-	-	-	-	-	-

Table 4.5: Data sample considered in this analysis. The center of mass energy is given in GeV. The luminosity is given in nb^{-1}. The total integrated luminosity is 155 pb^{-1}.

final state bremsstrahlung corrections, which in principle are missing completely in SCOT. In this case, however, only the longitudinal spin effects are considered and for the Lorentz structure of the neutral current, only the SM description is assumed.

Finally, the KORALB Monte Carlo [42] program has the complete description of the spin effects in tau production within the neutral current structure predicted by the SM. However, no bremsstrahlung correction is applied. This Monte Carlo program was used at the beginning of this analysis to verify the results obtained with SCOT within its scope.

In order to compare with the real data, a detector simulation is needed after the events are generated with one of the above Monte Carlo programs. This is done with GALEPH [43], a program in which all the information about the geometry and materials involved in the experimental setup of ALEPH is described. For the tracking simulation, the primary long–lived particles are followed through the detector. Secondary particles are also produced by interaction with the detector material.

4.7 Tau direction of flight

The reconstruction of the $\vec{h}$ vectors needs the tau flight direction, since the momenta of the decaying particles are expressed in the tau rest frame. The expressions for the $\vec{h}$ vectors are shown in appendix B.

For events in which both taus decay hadronically, two independent angles, $\theta_{h^{\pm}\tau^{\pm}}$,

between the $\tau^{\pm}$ and the corresponding hadron, can be determined by the following equation:

$$\cos(\theta_{h^{\pm}\tau^{\pm}}) = \frac{2E_{\tau}E_{h^{\pm}} - m_{\tau}^2 - m_{h_{\pm}}^2}{\sqrt{4(E_{\tau}^2 - m_{\tau}^2)(E_{h^{\pm}}^2 - m_{h_{\pm}}^2)}}, \tag{4.3}$$

where $E_{h^{\pm}}$ is the hadron energy in the laboratory frame. To obtain this expression, the energy and momenta conservation are used, and the following assumptions are made:

- the τ's are produced back–to–back with $E_{\tau^+} = E_{\tau^-} \equiv E_{\tau} = \sqrt{s}/2$ [1],
- $m_{\nu_{\tau}} = m_{\bar{\nu}_{\tau}} = 0$.

For each decay, the corresponding $\theta_{h^{\pm}\tau^{\pm}}$ angle determines a cone around the hadron momentum where the tau direction could lie. If one of the cones is inverted, the intersection of both surfaces determines two solutions (τ_1 and τ_2), as shown schematically in fig. 4.4.

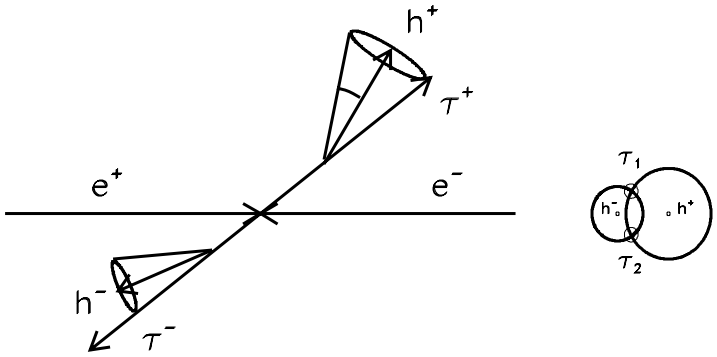

Figure 4.4: Geometric view of the τ flight direction reconstruction and the two possible solutions τ_1 and τ_2.

To express both solutions we choose the following unitary vectors:

$$\hat{n}_1 \;=\; \hat{n}_2 \times \hat{n}_3 = \frac{1}{\sin(\Delta\theta)} \left(\hat{p}_{h^-} - \hat{p}_{h^+} \cos(\Delta\theta)\right) ,$$

[1] Event by event, $\sqrt{s}/2$ is considered to be equal to the beam energy measured by LEP, in order to take into account variations of the center of mass energy from M_Z.

$$\begin{aligned} \hat{n}_2 &= \frac{1}{\sin(\Delta\theta)}(\hat{p_{h^-}} \times \hat{p_{h^+}}) \,, \\ \hat{n}_3 &= -\hat{p_{h^+}} \,, \end{aligned} \tag{4.4}$$

where $\cos(\Delta\theta) = \hat{p_{h^-}} \cdot \hat{p_{h^+}}$, and where the $\hat{p_{h^\pm}}$ are unitary vectors in the direction of the hadrons.

If we express the tau direction coordinates as $\hat{e}_\tau = a\hat{n}_1 + b\hat{n}_2 + c\hat{n}_3$, it turns out that

$$\begin{aligned} a &= \frac{1}{\sin(\Delta\theta)} \left(\cos(\theta_{h^-\tau^-}) + \cos(\theta_{h^+\tau^+}) \cos(\Delta\theta)\right) \,, \\ c &= \cos(\theta_{h^+\tau^+}) \,, \\ b &= \pm\sqrt{1 - a^2 - c^2} \,, \end{aligned} \tag{4.5}$$

where the two solutions correspond to the two signs of b.

The expression $1 - a^2 - c^2$ is not always greater than zero, due either to detector effects or to Initial State Radiation. In practice it is possible to reconstruct the two tau directions only for about 63% of the hadronic events.

For events with two tau directions, in principle, it could be possible to disentangle the good solution using the information of the vertex detector [44, 45]. By contrast, one of the methods to measure the tau polarisation at LEP I in ALEPH [46] has shown that this improvement is very small. Thus, we have preferred to average the information coming from each of the solutions in the fitting expression.

In this analysis we consider events with two reconstructed tau directions, and also an extra fraction of events in which the tau flight direction is obtained with a procedure developed for the measurement of the tau polarisation [46]. In this procedure, the particle momenta are fluctuated within their nominal errors 500 times, and the two possible solutions from the intersection of the two cones are tried to be determined each time. The event is accepted if the cones have intersected at least 10 times, and the tau direction is the average over all the solutions found.

Chapter 5

Likelihood function

In section 2.3, we introduced the likelihood function of this analysis from the theoretical point of view. Nevertheless, in reality some more elements have to be taken into account, such as the detector resolution and the presence of background. In this chapter we add these two effects to the likelihood function, in order to properly describe the event probability of a detected event.

5.1 Likelihood formalism

The theoretical likelihood function was written in section 2.3 for the decay topology (ij) as the following product:

$$L_{id}(\mu_\tau, d_\tau|\Omega, W_1, \cos\theta_{h_1}, \phi_{h_1}, W_2, \cos\theta_{h_2}, \phi_{h_2}) = \bar{R}_{\mu\nu}(\mu_\tau, d_\tau, \Omega)\bar{H}_i^\mu(W_1, \cos\theta_{h_1}, \phi_{h_1})\bar{H}_j^\nu(W_2, \cos\theta_{h_2}, \phi_{h_2}) \,,$$

with

$$\begin{aligned} \bar{R}_{\mu\nu}(\mu_\tau, d_\tau, \Omega) &= \frac{R_{\mu\nu}(\mu_\tau, d_\tau, \Omega)}{|A|^2(\mu_\tau, d_\tau, \Omega)} \,, \\ \bar{H}^\mu(W, \cos\theta_h, \phi_h) &= \frac{W h^\mu}{\Gamma_\tau} \,. \end{aligned} \tag{5.1}$$

The normalization is such that

$$\sum_{ij} \int L_{ij}(\mu_\tau, d_\tau|\Omega, W_1, \cos\theta_{h_1}, \phi_{h_1}, W_2, \cos\theta_{h_2}, \phi_{h_2}) d\bar{X}_1 d\bar{X}_2 = 1 \,. \tag{5.2}$$

And the event observables are (W_1, $\cos\theta_{h_1}$, ϕ_{h_1}, W_2, $\cos\theta_{h_2}$, ϕ_{h_2}).

Nevertheless, two effects have always to be considered to properly describe the event probability: the detector effects and the background. The former may be treated by convoluting the likelihood function with a multidimensional resolution function, taking into account the possible true values of the observables given certain measurements. The latter are introduced in the fitting formula by correctly weighting their contributions.

Formally, the event probability for the decay topology (ij) is given by [1, 2]

$$\begin{aligned} L_{ij} &= \int \bar{R}_{\mu\nu}(\mu_\tau, d_\tau|\Omega)\bar{H}_i^\mu(W_1^{(0)}, \cos\theta_{h_1}^{(0)}, \phi_{h_1}^{(0)})\bar{H}_j^\nu(W_2^{(0)}, \cos\theta_{h_2}^{(0)}, \phi_{h_2}^{(0)}) \times \\ &\quad T_{ij}(W_1, \cos\theta_{h_1}, \phi_{h_1}, W_2, \cos\theta_{h_2}, \phi_{h_2}, W_1^{(0)}, \cos\theta_{h_1}^{(0)}, \phi_{h_1}^{(0)}, W_2^{(0)}, \cos\theta_{h_2}^{(0)}, \phi_{h_2}^{(0)}) \times \\ &\quad dW_1^{(0)} d\cos\theta_{h_1}^{(0)} d\phi_{h_1}^{(0)} dW_2^{(0)} d\cos\theta_{h_2}^{(0)} d\phi_{h_2}^{(0)} + \text{Background} , \end{aligned}$$

where T is the resolution function describing the probability that an event produced with "true" values $(W_1^{(0)}, \cos\theta_{h_1}^{(0)}, \phi_{h_1}^{(0)}, W_2^{(0)}, \cos\theta_{h_2}^{(0)}, \phi_{h_2}^{(0)})$ is observed with the measured values $(W_1, \cos\theta_{h_1}, \phi_{h_1}, W_2, \cos\theta_{h_2}, \phi_{h_2})$.

To calculate the resolution function in ten dimensions is almost impossible and, therefore, some simplifications have to be applied. We will write the likelihood for each event as

$$\begin{aligned} L_{ij} &= \int \bar{R}_{\mu\nu}(\mu_\tau, d_\tau|\Omega)\bar{H}_i^\mu(W_1^{(0)}, \cos\theta_{h_1}^{(0)}, \phi_{h_1}^{(0)})\bar{H}_j^\nu(W_2^{(0)}, \cos\theta_{h_2}^{(0)}, \phi_{h_2}^{(0)}) \times \\ &\quad D_i(W_1 - W_1^{(0)}, W_1^{(0)}) D_i(\cos\theta_{h_1} - \cos\theta_{h_1}^{(0)}, \cos\theta_{h_1}^{(0)}) D_i(\phi_{h_1} - \phi_{h_1}^{(0)}, \phi_{h_1}^{(0)}) \times \\ &\quad D_j(W_2 - W_2^{(0)}, W_2^{(0)}) D_j(\cos\theta_{h_2} - \cos\theta_{h_2}^{(0)}, \cos\theta_{h_2}^{(0)}) D_j(\phi_{h_2} - \phi_{h_2}^{(0)}, \phi_{h_2}^{(0)}) \times \\ &\quad \epsilon_i(\cos\theta_{h_1}^{(0)}) \epsilon_j(\cos\theta_{h_2}^{(0)}) dW_1^{(0)} d\cos\theta_{h_1}^{(0)} d\phi_{h_1}^{(0)} dW_2^{(0)} d\cos\theta_{h_2}^{(0)} d\phi_{h_2}^{(0)} . \end{aligned} \tag{5.3}$$

The convolution of the detector effects with the event probability is factored for each of the decays separately, and, for each decay, into three smearing functions ($D(x - x^{(0)}, x^{(0)})$ in the formula, with $x = W, \cos\theta_h, \phi_h$), one for each of the three event observables per hemisphere (W, $\cos\theta_h$, ϕ_h). These functions describe the smearing effect of the detector for accepted events. There is also an overall efficiency

[1] In principle the production angle Ω should also be part of the resolution function, although in practice, as long as the anomalous coupling terms are near zero, the resolution on Ω can be safely neglected [6].

[2] The $\bar{R}_{\mu\nu}$ terms are also functions of the event center of mass energy ($\sqrt{s}$), as shown in appendix A. This dependence is evaluated, for each event, by taken $\sqrt{s} = 2E_{beam}$, where E_{beam} is the beam energy measured by LEP.

function (ϵ) describing the probability that a given "true" event will actually pass the tau selection criteria. We will come back later to the possible dependence of the efficiency on more "true" variables.

Eq. 5.3 takes as independent statistical variables $x - x^{(0)}$ and $y - y^{(0)}$, with $x, y = W, \cos\theta_h, \phi_h$ and $x \neq y$. It also assumes $x - x^{(0)}$ and $y^{(0)}$ to be uncorrelated quantities, with x and y taking the same values as before. We will see later that in the final expressions we do take into account certain correlations between the above variables.

5.2 Smearing functions

In this section, we explain how to determine $D(x - x^{(0)}, x^{(0)})$. In what follows, x will be either W, $\cos\theta_h$ or ϕ_h.

For each channel, $D(x - x^{(0)}, x^{(0)})$ is a two dimensional function describing the probability that the smearing introduced by the detector is $(x - x^{(0)})$ for a certain generated $x^{(0)}$ with reconstructed x. Therefore, we calculate $D(x - x^{(0)}, x^{(0)})$ within the acceptance region for $x^{(0)}$. If we define $e \equiv x - x^{(0)}$, it follows from the definition that

$$\int D(e, x^{(0)}) de = 1 \,. \tag{5.4}$$

This normalization is possible because, when obtaining $D(x - x^{(0)}, x^{(0)})$, each $x^{(0)}$ has associated a certain x. The efficiency of the detector is handled by a separate function, the ϵ introduced before.

The $D(x - x^{(0)}, x^{(0)})$ functions are obtained with the Monte Carlo simulation, where the probability density functions of x ($\equiv f_x(x)$) and of $x^{(0)}$ ($\equiv f_{x^{(0)}}(x^{(0)})$) are known. $D(x - x^{(0)}, x^{(0)})$ are calculated by binning the $(x - x^{(0)}, x^{(0)})$ plane and applying the normalization of eq. 5.4 in each bin of $x^{(0)}$. The final two dimensional binning is determined for each smearing function by requiring that

$$f_x(x) = \int D(x - x^{(0)}, x^{(0)}) f_{x^{(0)}}(x^{(0)}) dx^{(0)} \,, \tag{5.5}$$

which express the convolution of $f_{x^{(0)}}(x^{(0)})$ with the fluctuations introduced by the detector.

Smearing function for W

The $D(W - W^{(0)}, W^{(0)})$ functions are calculated for, typically, 600 bins in $W - W^{(0)}$ and 200 bins in $W^{(0)}$. This binning is such that eq. 5.5 is satisfied as mentioned before.

To illustrate the shape of the smearing functions for W, fig. 5.1 presents $D(W - W^{(0)}, W^{(0)})$ in just very coarse bins of $W^{(0)}$ for the ρ channel. The behaviour of the $D(W - W^{(0)}, W^{(0)})$ function for the $\pi 2\pi^0$ and the 3π channels is very similar to that of the ρ. For the pion decay, the differential partial width is a constant for unpolarised taus, and thus, $W^{(0)}$ is a known number.

The dependence of $D(W - W^{(0)}, W^{(0)})$ on more variables has also been studied and has been found to be negligible.

Smearing function for the polarimeter polar angle

The $D(\cos\theta_h - \cos\theta_h^{(0)}, \cos\theta_h^{(0)})$ functions are calculated for typically 120 bins in $(\cos\theta_h - \cos\theta_h^{(0)})$ and 50 bins in $\cos\theta_h^{(0)}$. However, this function increases very sharply for the ρ, $\pi 2\pi^0$ and 3π channels for values of $\cos\theta_h^{(0)}$ very close to $\pm$ 1; and therefore we have applied a much finer binning in those regions (about 1400 bins are taken on $(\cos\theta_h - \cos\theta_h^{(0)})$) for those channels.

Figs. 5.2, 5.3, 5.4, 5.5 show the $D(\cos\theta_h - \cos\theta_h^{(0)}, \cos\theta_h^{(0)})$ functions in four coarse bins of $\cos\theta_h^{(0)}$ for the four channels considered.

In each of these plots, every event contributes twice: once for each of the two available tau directions per event. On the contrary, in the case of the pion decay channel, the polar angle of the polarimeter is uniquely determined for both experimentally available tau directions. This is a very important feature coming from the two body decay type.

The behaviour of the smearing functions is as expected for the pion channel: the negative $\cos\theta_h^{(0)}$ values corresponds to high pion energies, where the energy determination is poorer. For the other channels, there is a tail which is a function of $\cos\theta_h^{(0)}$; however, the width of the curves around the peak is not simple to explain, since the polarimeter expression is more complicated for those cases and the detector effects are not easy to trace.

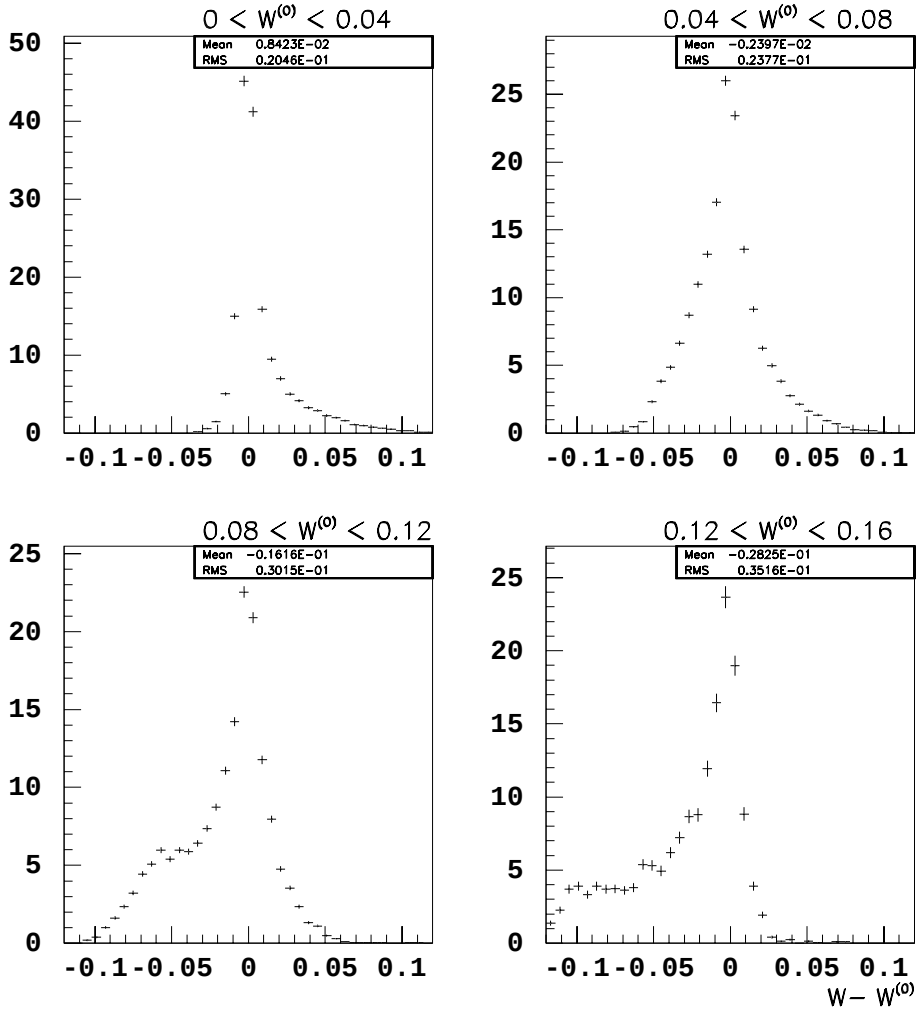

Figure 5.1: Smearing function of the W variable for the ρ channel in just four coarse bins of $W^{(0)}$.

Smearing function for the polarimeter azimuthal angle

The $D(\phi_h - \phi_h^{(0)}, \phi_h^{(0)})$ functions are found not to depend on $\phi_h^{(0)}$, because ϕ_h is a periodical variable and the detector is symmetric in this angle. In what follows we then omit the second argument.

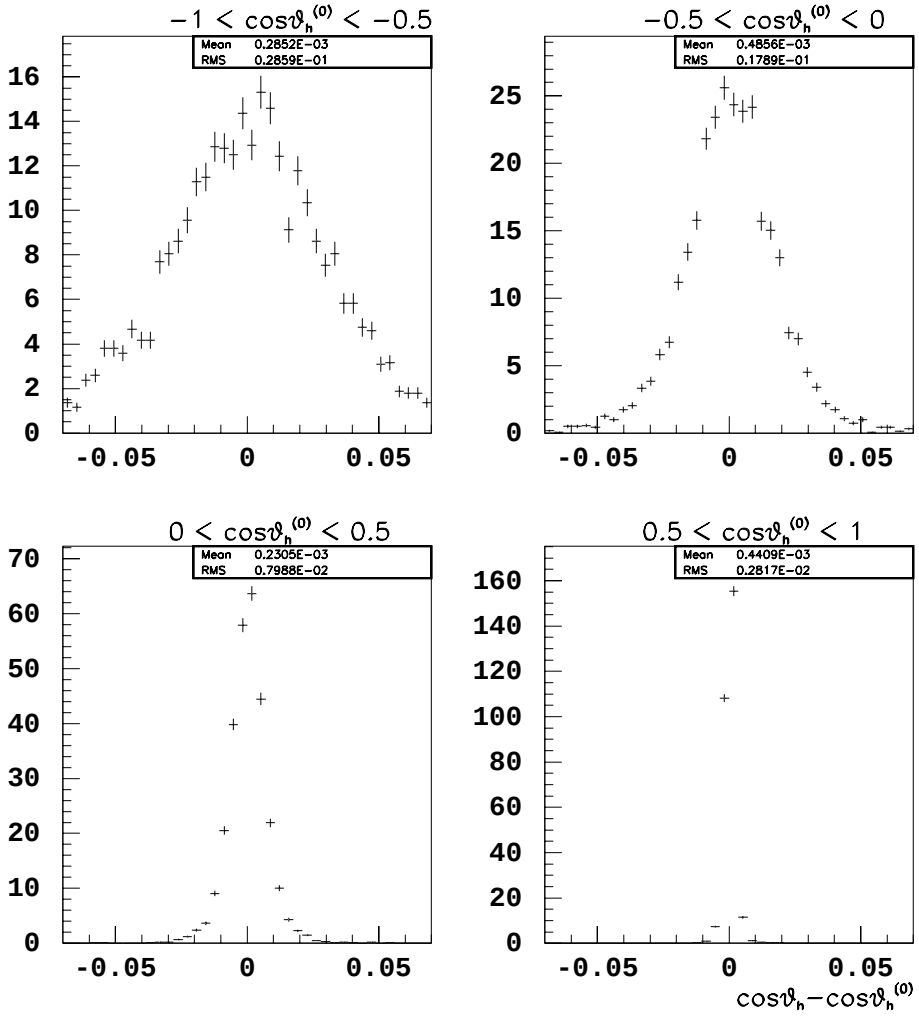

Figure 5.2: Smearing functions of the polarimeter polar angle for the pion channel in just four coarse bins of $\cos\theta_h^{(0)}$.

It has also been verified that

$$f_{\phi_h}(\phi_h) = \int D(\phi_h - \phi_h^{(0)}) f_{\phi_h^{(0)}}(\phi_h^{(0)}) d\phi_h^{(0)} \ . \tag{5.6}$$

However, we have empirically found that $(\phi_h - \phi_h^{(0)})$ is correlated with $\cos\theta_h$; and then have calculated $D(\phi_h - \phi_h^{(0)})$ in various bins of $\cos\theta_h$ (typically 10), checking that eq. 5.6 is verified in each bin of $\cos\theta_h$.

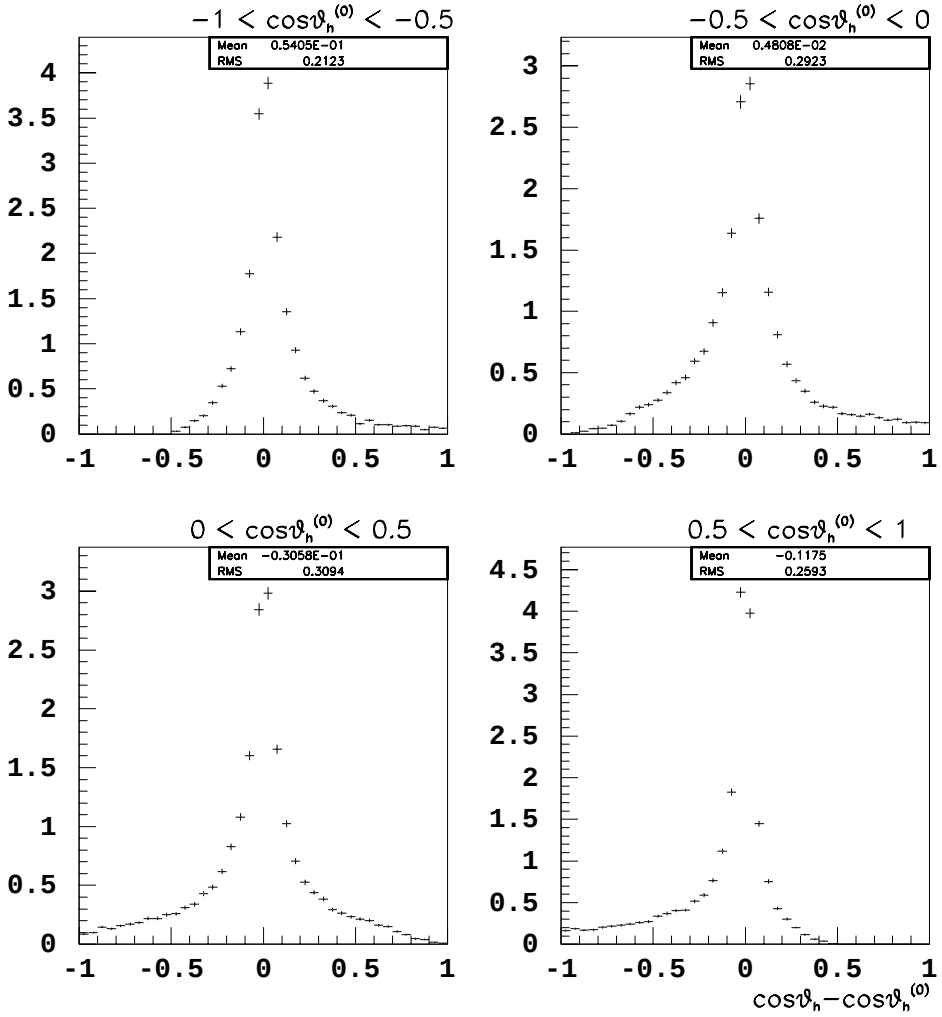

Figure 5.3: Smearing functions of the polarimeter polar angle for the rho channel in just four coarse bins of $\cos\theta_h^{(0)}$.

We illustrate the behaviour of $D(\phi_h - \phi_h^{(0)}, \cos\theta_h)$, for the four channels considered, in figs. 5.6, 5.7, 5.8, 5.9, in which just four coarse bins of $\cos\theta_h$ are taken.

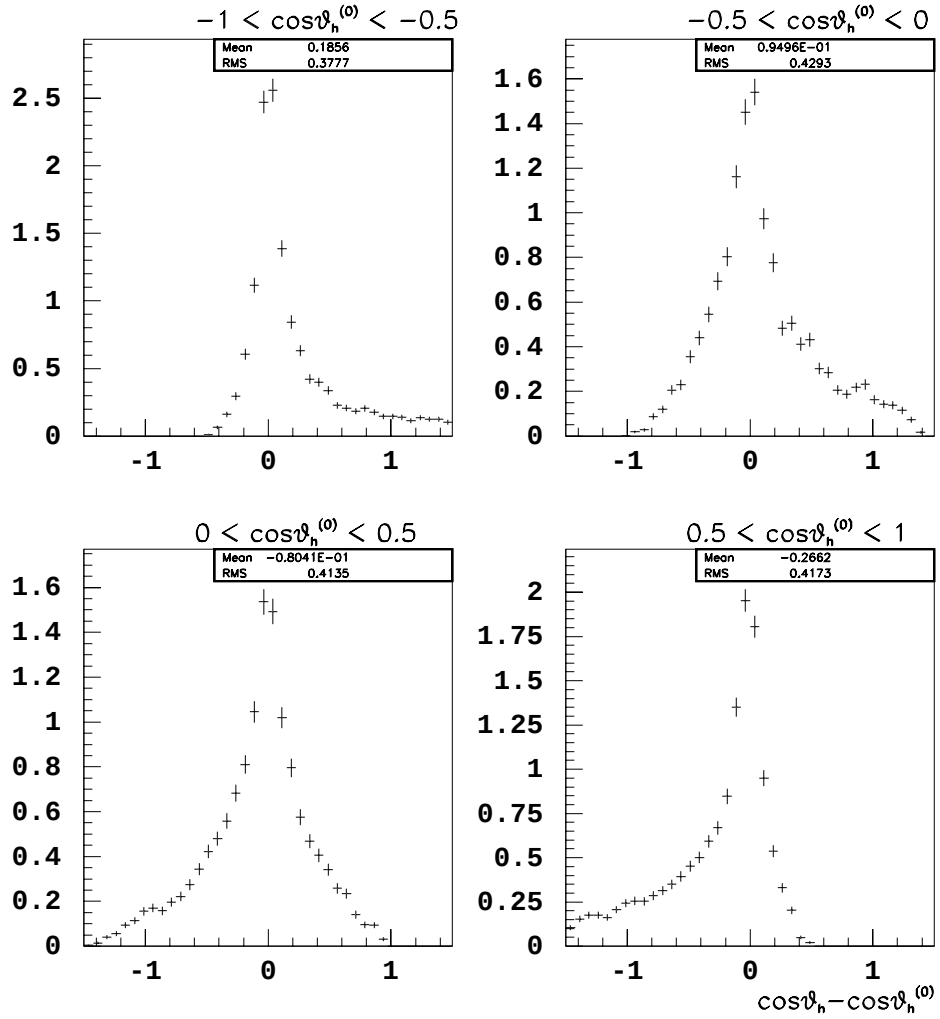

Figure 5.4: Smearing functions of the polarimeter polar angle for the $\pi 2\pi^0$ channel in just four coarse bins of $\cos\theta_h^{(0)}$.

5.3 Detection Efficiency

As shown in eq. 5.3, the efficiency is handled with the $\epsilon(\cos\theta_h^{(0)})$ function. In this context, the smearing functions can be calculated within the acceptance region of the generated variables.

In practice, we introduce a matrix of efficiencies, i.e. $\epsilon_{ij}(\cos\theta_h^{(0)})$, which is the

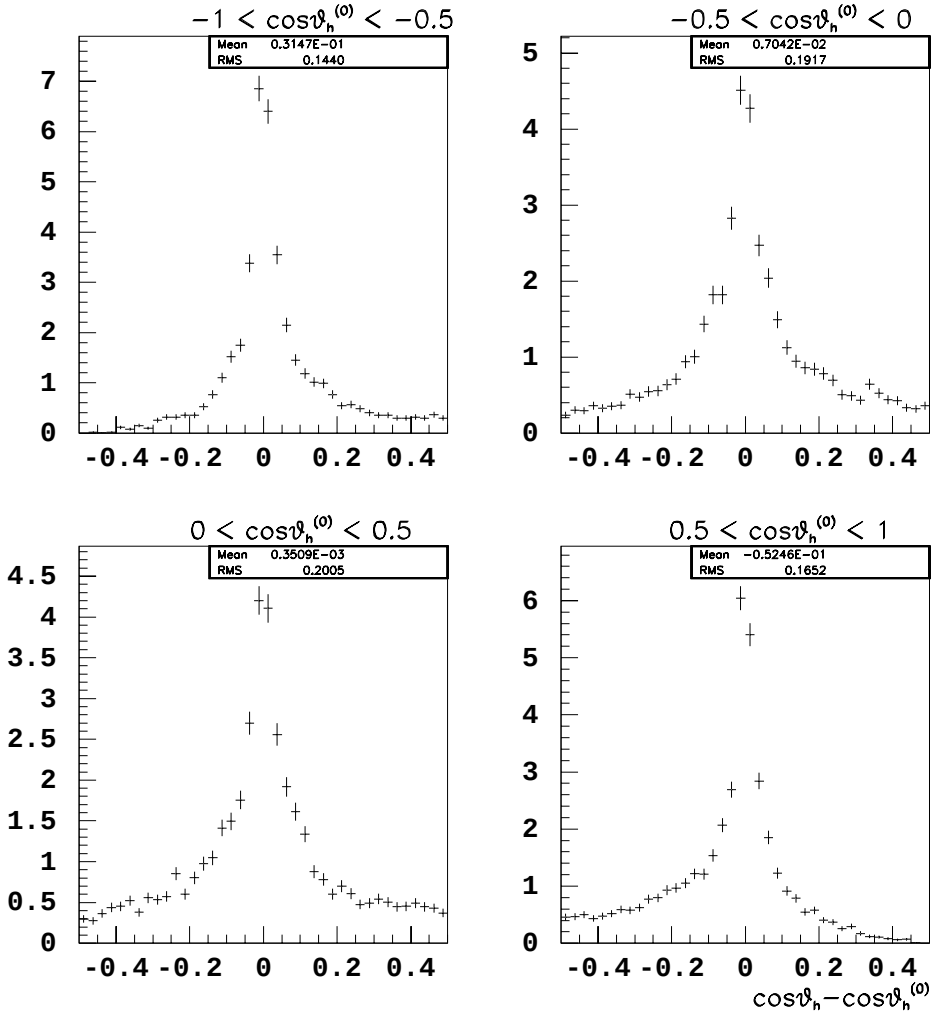

Figure 5.5: Smearing function of the polarimeter polar angle for the 3π channel in just four coarse bins of $\cos\theta_h^{(0)}$.

probability that a generated event in the topology i is identified as j. In principle, this function could depend on $W^{(0)}$, on $\cos\theta_h^{(0)}$ and on $\phi_h^{(0)}$. On the contrary, the dependence on the azimuthal angle is very flat and, furthermore, any possible effect from $W^{(0)}$ or $\phi_h^{(0)}$ on the final result could be treated as a systematic error. It should be also noticed that the $\epsilon_{ij}(\cos\theta_h^{(0)})$ function includes both the probability of selecting an event and the probability of correctly identifying it.

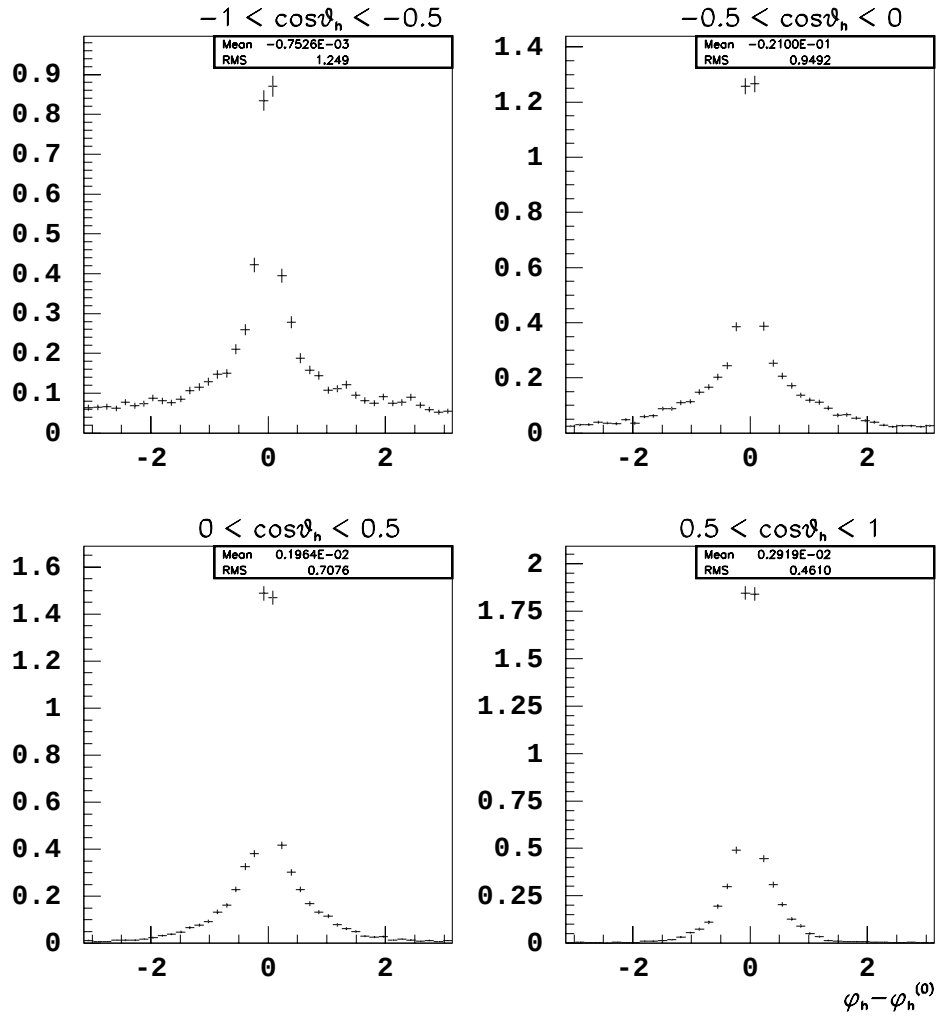

Figure 5.6: Smearing functions of the polarimeter azimuthal angle for the pion channel in four coarse bins of $\cos\theta_h$.

The efficiency matrix $\epsilon_{ij}(\cos\theta_h^{(0)})$ has been calculated separately in the barrel ($|\cos\theta| < 0.75$) and in the end–cap region (the remainder), where the performance of the detector degrades. These functions are shown in figs. 5.10 and 5.11. In both cases, the efficiencies are quite uniform for the diagonal elements, where the identification is correct. In the off–diagonal elements, the generated events are mis–identified within one of the categories considered. It can be seen that the rate of

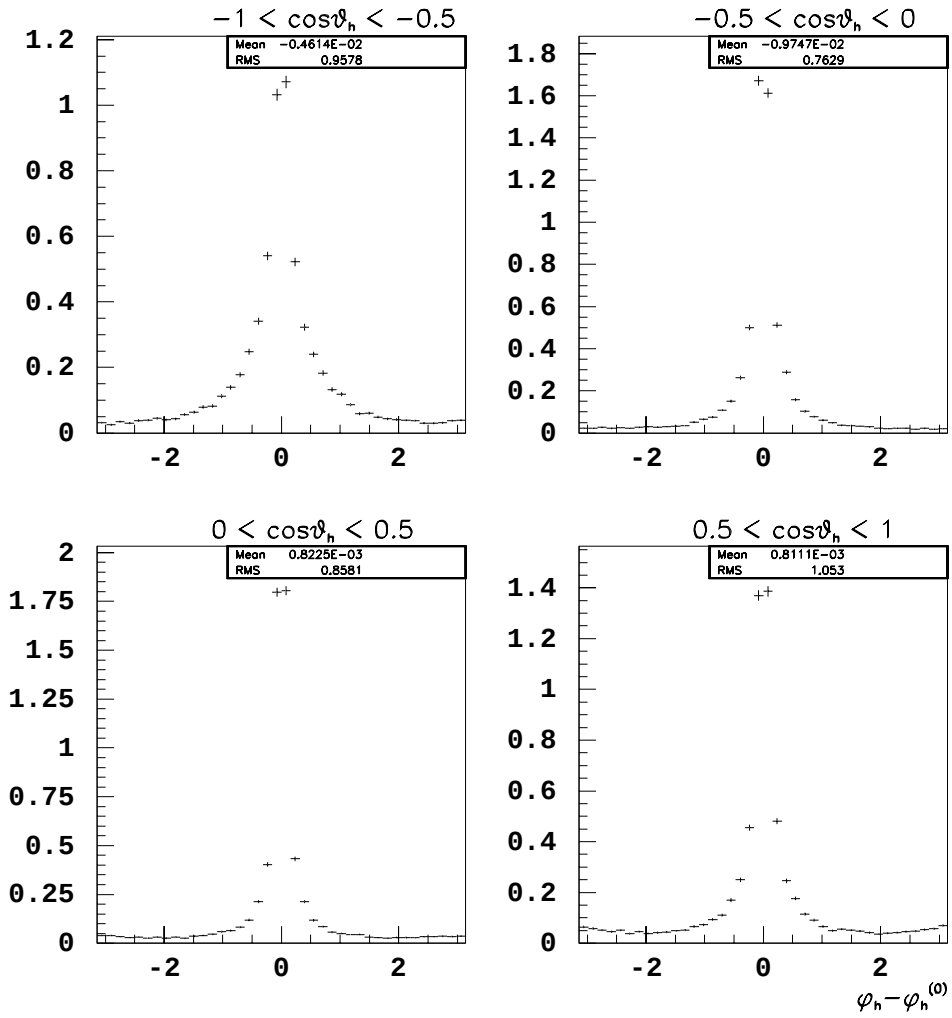

Figure 5.7: Smearing function of the polarimeter azimuthal angle for the rho channel in four coarse bins of $\cos\theta_h$.

mis–identification of these off–diagonal elements is in, most cases, negligible, despite the relevant contamination of $\pi 2\pi^0$ into ρ (about 7% in the barrel and 5% in the end–cap). In fig. 5.12, we present the efficiency for miss–identification of other tau decays within one of the categories considered, for the barrel and the end–cap regions. The rate is very small for both regions and for all the channels.

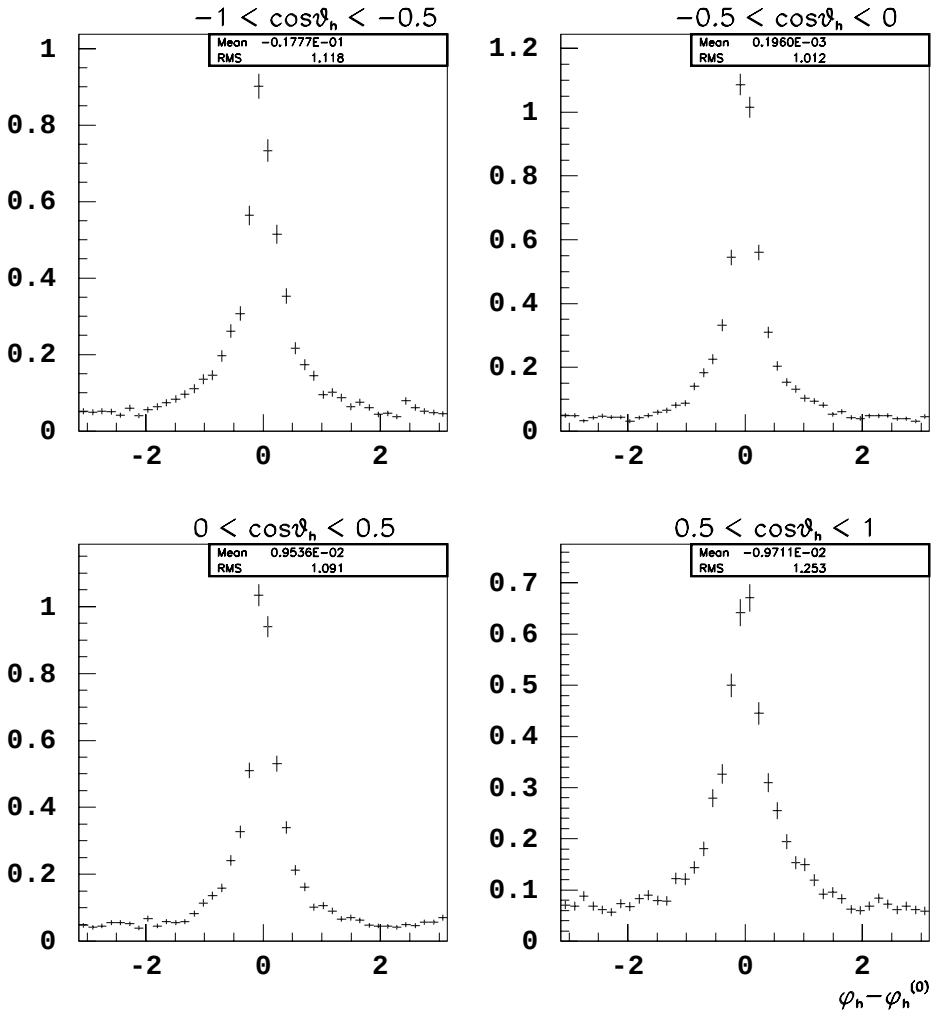

Figure 5.8: Smearing functions of the polarimeter azimuthal angle for the $\pi 2\pi^0$ channel in four coarse bins of $\cos\theta_h$.

5.4 Effective $\tilde{H}$ functions

The convolution of the theoretical likelihood function over the detector smearing and efficiency functions described by eq. 5.3 is only dependent upon the observed decay properties of the identified hemisphere. This convolution can be re–written

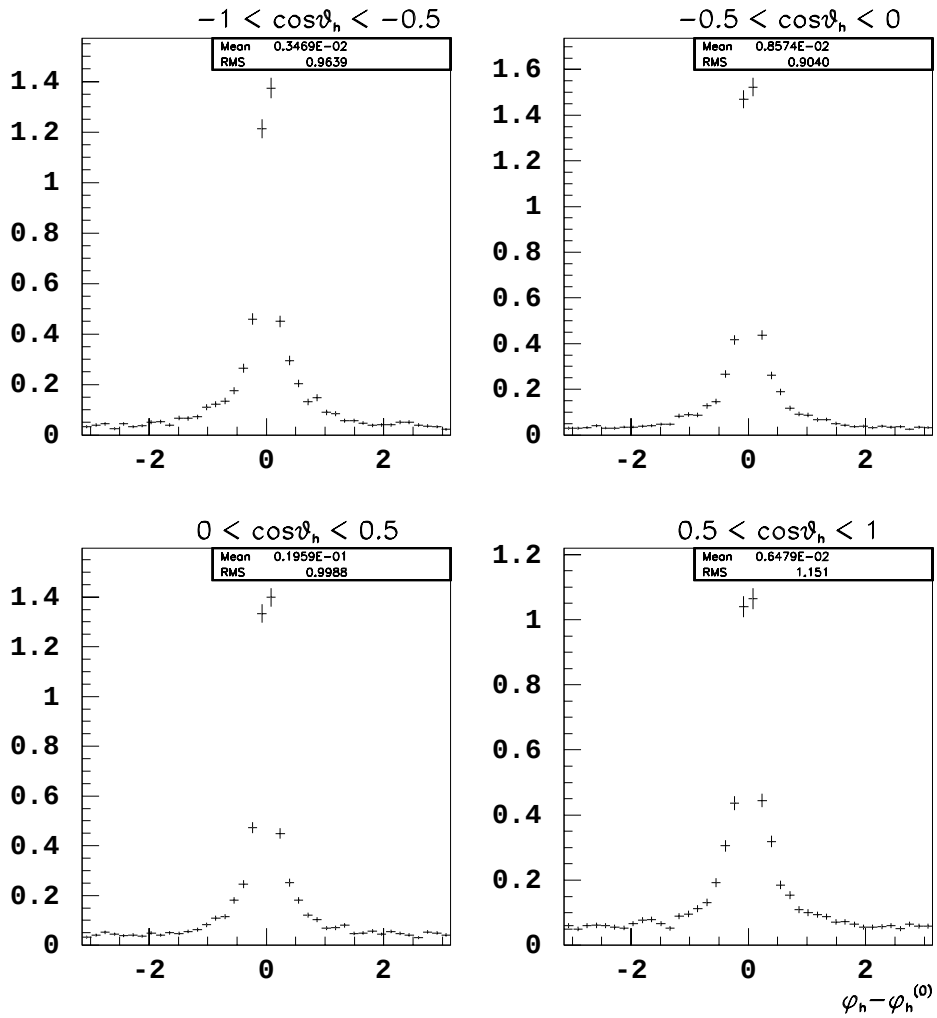

Figure 5.9: Smearing functions of the polarimeter azimuthal angle for the 3π channel in four coarse bins of $\cos\theta_h^{(0)}$.

in terms of the effective $\tilde{H}$ functions as

$$\tilde{H}_i^{\mu}(W,\cos\theta_h,\phi_h) = \int \bar{H}_i^{\mu}(W^{(0)},\cos\theta_h^{(0)},\phi_h^{(0)}) \times$$
$$D_i(W-W^{(0)},W^{(0)})D_i(\cos\theta_h-\cos\theta_h^{(0)},\cos\theta_h^{(0)})D_i(\phi_h-\phi_h^{(0)},\cos\theta_h) \times$$
$$\epsilon_i(\cos\theta_h^{(0)})dW^{(0)}d\cos\theta_h^{(0)}d\phi_h^{(0)} \ , \qquad (5.7)$$

where the $\epsilon_i(\cos\theta_h^{(0)}) \equiv \epsilon_{ii}(\cos\theta_h^{(0)})$.

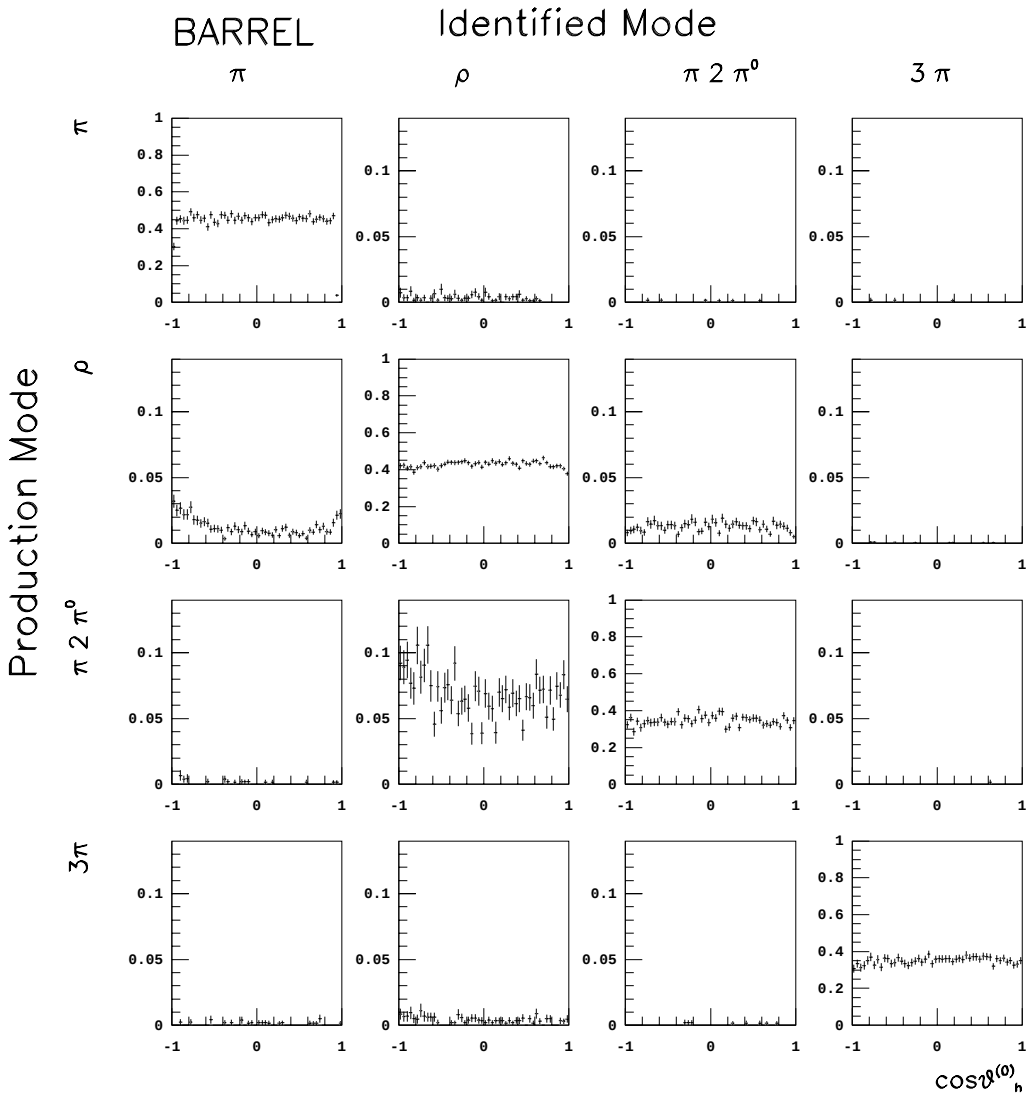

Figure 5.10: Efficiency function $\epsilon_{ij}(\cos\theta_h^{(0)})$ as a function of the generated polar angle of the polarimeter in the barrel region.

The $\bar{H}_i^{\mu}$ functions are recalled in eq. 5.1, and are related with the polarimeter of each decay, the $\vec{h}$ vector (explicitly written in appendix B for the decay modes considered).

The great advantage of factoring the likelihood function in this manner is that the integrals of eq. 5.7 are calculated only once, because the effective $\tilde{H}$ functions for each observed hemisphere are completely independent of the anomalous couplings,

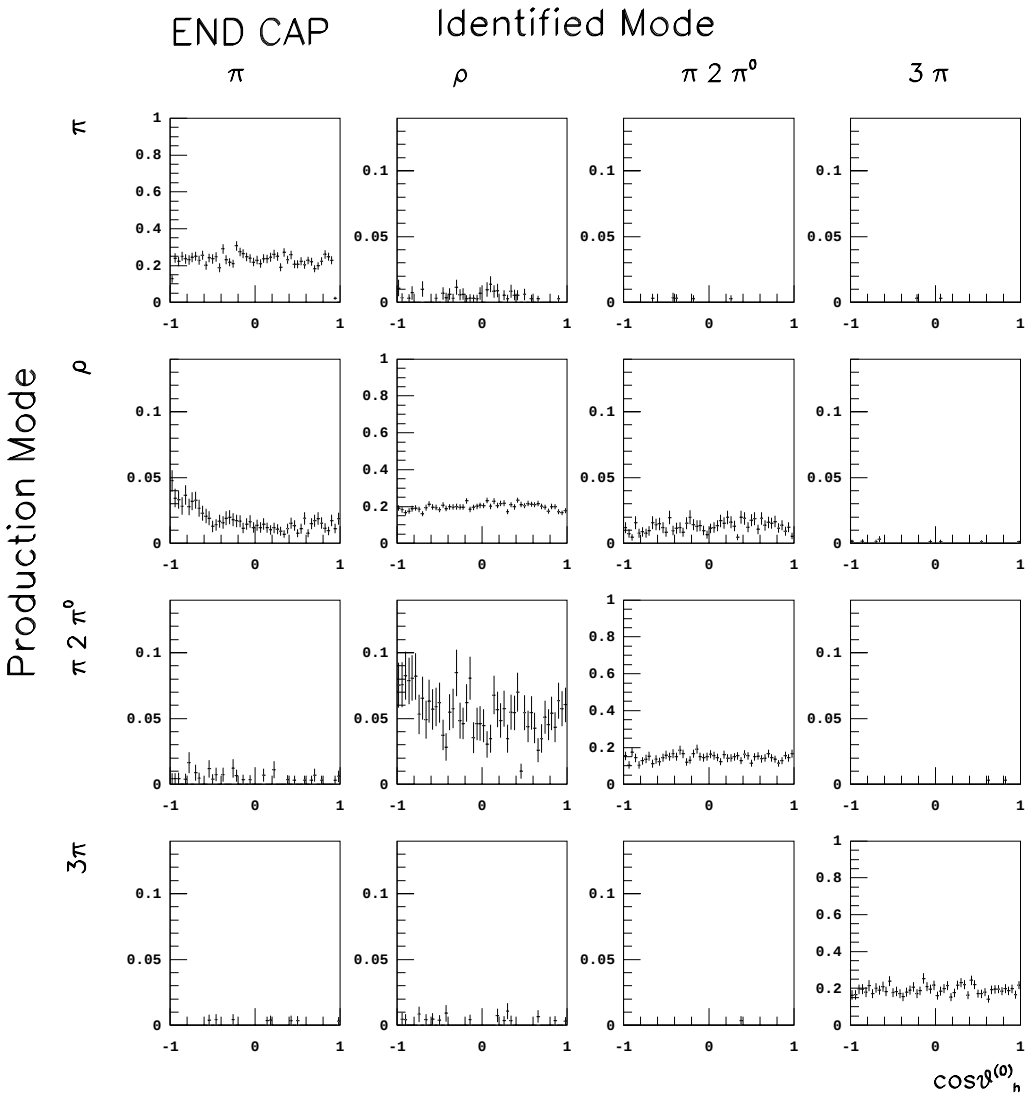

Figure 5.11: Efficiency function $\epsilon_{ij}(\cos\theta_h^{(0)})$ as a function of the generated polar angle of the polarimeter in the end–cap region.

which are iterated over in the likelihood fit.

5.5 Background

The sample of data we have is very pure, but a few unwanted events are remaining, which are handled in different ways depending on their source. We classify the

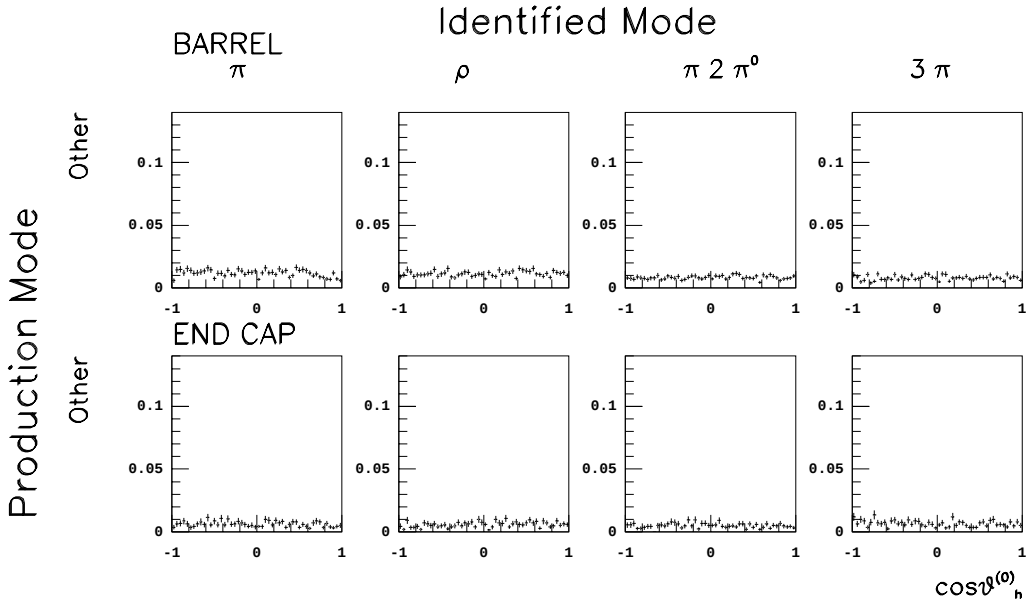

Figure 5.12: Efficiency function for mis–identifying any tau decay not used in this analysis (*other*) within one of the categories considered, for the barrel (top) and the end–cap region (bottom).

background in the following types:

- Mis–identified spin–sensitive tau decay modes.
- Other mis–identified tau decay modes.
- Background from non–tau sources.

All sources of background can be accommodated into the likelihood formalism by expanding the effective $\tilde{H}$ functions of eq. 5.7. In this sense, the $\tilde{H}$ describe a weighted sum of the expected components in each identified decay channel. For each hemisphere identified in channel j, the complete effective $\tilde{H}$ function is then given by

$$\tilde{H}^{\mu}_{j}(W, \cos\theta_h, \phi_h) = \sum_{i} \tilde{H}^{\mu}_{ij}(W, \cos\theta_h, \phi_h)\,. \tag{5.8}$$

The index i runs over the four identified tau hemisphere types, the background from other tau decay modes, as well as the non–tau background sources. The new $\tilde{H}^{\mu}_{ij}(W, \cos\theta_h, \phi_h)$ functions are written for the three types of background at length.

Spin–sensitive tau background

We consider as mis–identified spin–sensitive tau background those events mis–identified within one of the decay modes considered for this analysis. The effective $\tilde{H}^{\mu}_{ij}(W, \cos\theta_h, \phi_h)$ functions are written for them as

$$\tilde{H}^{\mu}_{ij}(W, \cos\theta_h, \phi_h) = \int \bar{H}^{\mu}_{i}(W^{(0)}, \cos\theta_h^{(0)}, \phi_h^{(0)}) \times$$
$$D_{ij}(W - W^{(0)}, W^{(0)}) D_{ij}(\cos\theta_h - \cos\theta_h^{(0)}, \cos\theta_h^{(0)}) D_{ij}(\phi_h - \phi_h^{(0)}, \cos\theta_h) \times$$
$$\epsilon_{ij}(\cos\theta_h^{(0)}) dW^{(0)} d\cos\theta_h^{(0)} d\phi_h^{(0)} \; . \tag{5.9}$$

The most relevant change with respect to eq. 5.7 is that we introduce the smearing functions for mis–identified events $D_{ij}(x - x^{(0)}, x^{(0)})$, with x=W, $\cos\theta_h$, ϕ_h. These functions express the probability to find $(x - x^{(0)})$ for accepted events which were generated with value $x^{(0)}$ and of type i but reconstructed with value x and of type j. Defining $e \equiv x - x^{(0)}$, it is verified that

$$\int D_{ij}(e, x^{(0)}) de = 1 \; . \tag{5.10}$$

This normalization is possible because the efficiency is handled with a separate function, the $\epsilon_{ij}(\cos\theta_h^{(0)})$ matrix, which, as said before, gives the probability that an event of type i is reconstructed as one of type j.

The $D_{ij}(x - x^{(0)}, x^{(0)})$ functions are also calculated binning the $(x - x^{(0)}, x^{(0)})$ plane and requiring that eq. 5.5 has to be satisfied.

$D_{ij}(\cos\theta_h - \cos\theta_h^{(0)}, \cos\theta_h^{(0)})$ and $D_{ij}(W - W^{(0)}, W^{(0)})$ are calculated in a similar way to the case of correctly identified events. $D_{ij}(\phi_h - \phi_h^{(0)}, \phi_h^{(0)})$ are also found not to depend on $\phi_h^{(0)}$ for the same reasons as before, and are calculated in four bins of $\cos\theta_h$ for the relevant background, i. e. for the contaminations of ρ into π, ρ into $\pi 2\pi^0$ and $\pi 2\pi^0$ into ρ.

For the ρ $\pi 2\pi^0$ mixing, we present $\int D_{ij}(W - W^{(0)}, W^{(0)}) dW^{(0)}$ in fig. 5.13. $D_{\rho\ \pi 2\pi^0}(\cos\theta_h - \cos\theta_h^{(0)}, \cos\theta_h^{(0)})$ and $D_{\pi 2\pi^0\ \rho}(\cos\theta_h - \cos\theta_h^{(0)}, \cos\theta_h^{(0)})$ are shown, for coarse bins of $\cos\theta_h^{(0)}$, in figs. 5.14 and 5.15. Finally, $D_{\rho\ \pi 2\pi^0}(\phi_h - \phi_h^{(0)}, \cos\theta_h)$ and $D_{\pi 2\pi^0\ \rho}(\phi_h - \phi_h^{(0)}, \cos\theta_h)$ can be found in figs. 5.16 and 5.17.

Eq. 5.9 is also different from eq. 5.7 in the inclusion of the off–diagonal elements of the $\epsilon_{ij}(\cos\theta_h^{(0)})$ matrix, which has been justified in the previous paragraphs.

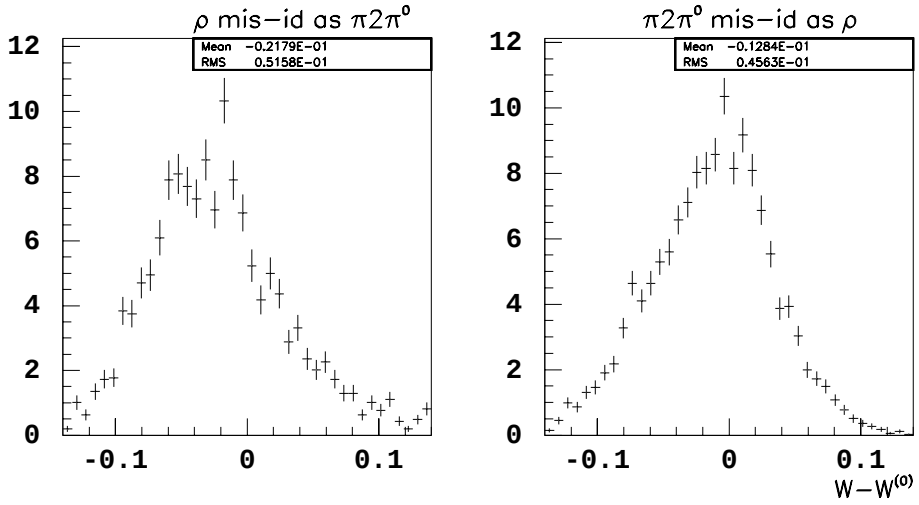

Figure 5.13: $\int D_{\rho\,\pi 2\pi^0}(W - W^{(0)}, W^{(0)})dW^{(0)}$ (left) and $\int D_{\pi 2\pi^0\,\rho}(W - W^{(0)}, W^{(0)})dW^{(0)}$ (right).

Other tau background

The remaining mis–identified tau decays are treated similarly to the previous background. The effective $\tilde{H}^{\mu}_{ij}(W, \cos\theta_h, \phi_h)$ functions are exactly those of eq. 5.9, with the $D_{other\,j}(x - x^{(0)}, x^{(0)})$ functions being extracted from the Monte Carlo simulation, as done for the spin–sensitive background. In principle, one can think that the $D_{other\,j}(x - x^{(0)}, x^{(0)})$ may be approximated by uniform distributions (which would mean a complete dilution of the underlying spin dependence). On the contrary, this hypothesis is not correct at all. In fig. 5.18, we present $\int D_{other\,j}(\cos\theta_h - \cos\theta_h^{(0)}, cos\theta_h^{(0)})dcos\theta_h^{(0)}$, $D_{other\,j}(\phi_h - \phi_h^{(0)})$ and $\int D_{other\,j}(W - W^{(0)}, W^{(0)})dW^{(0)}$, for $j = \rho$.

In eq. 5.9, the mis–identification efficiencies are $\epsilon_{other\,j}(\cos\theta_h^{(0)})$, which were introduced before.

Non–tau background

The background contribution from non–tau sources is clearly spin–independent and, thus, can be treated as a constant dilution of the effective spin density matrix.

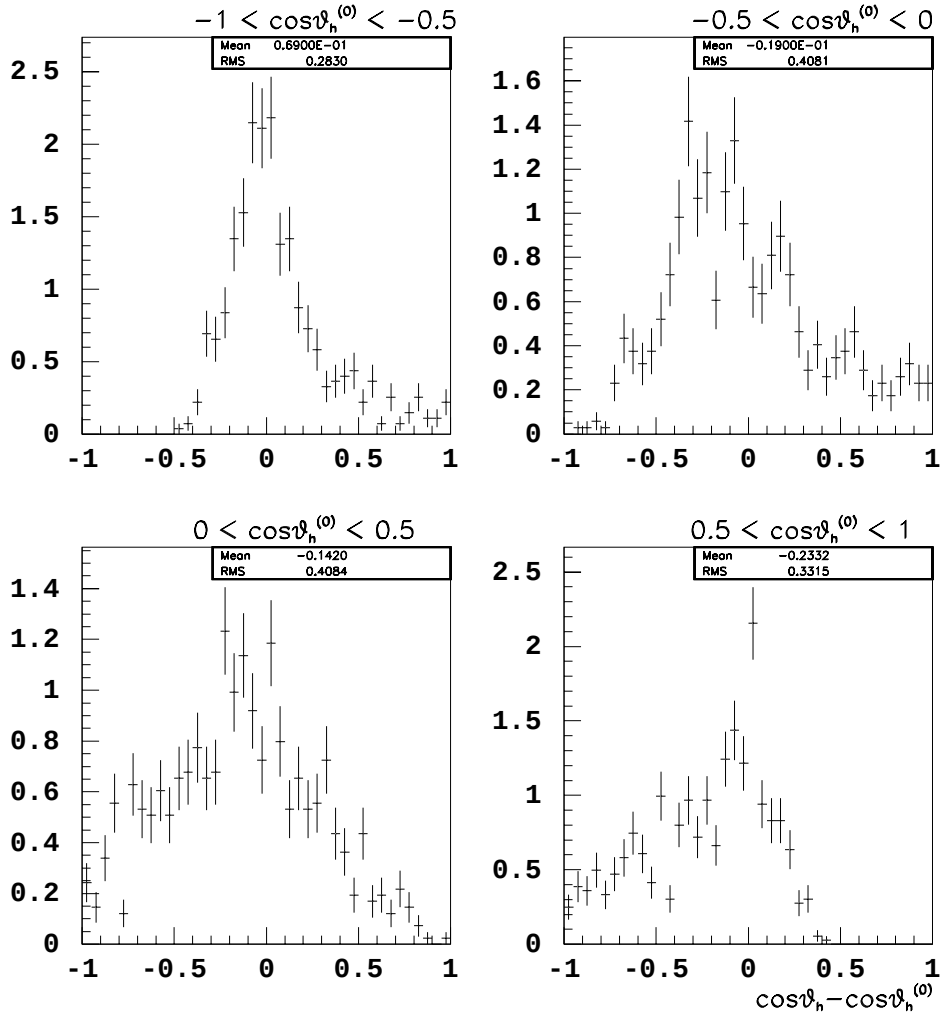

Figure 5.14: Smearing function of the polarimeter polar angle for ρ channels mis–identified as $\pi 2\pi^0$, in four coarse bins of $\cos\theta_h^{(0)}$.

Nevertheless, we do not need to introduce any correction for it, since the amount of this background is completely negligible.

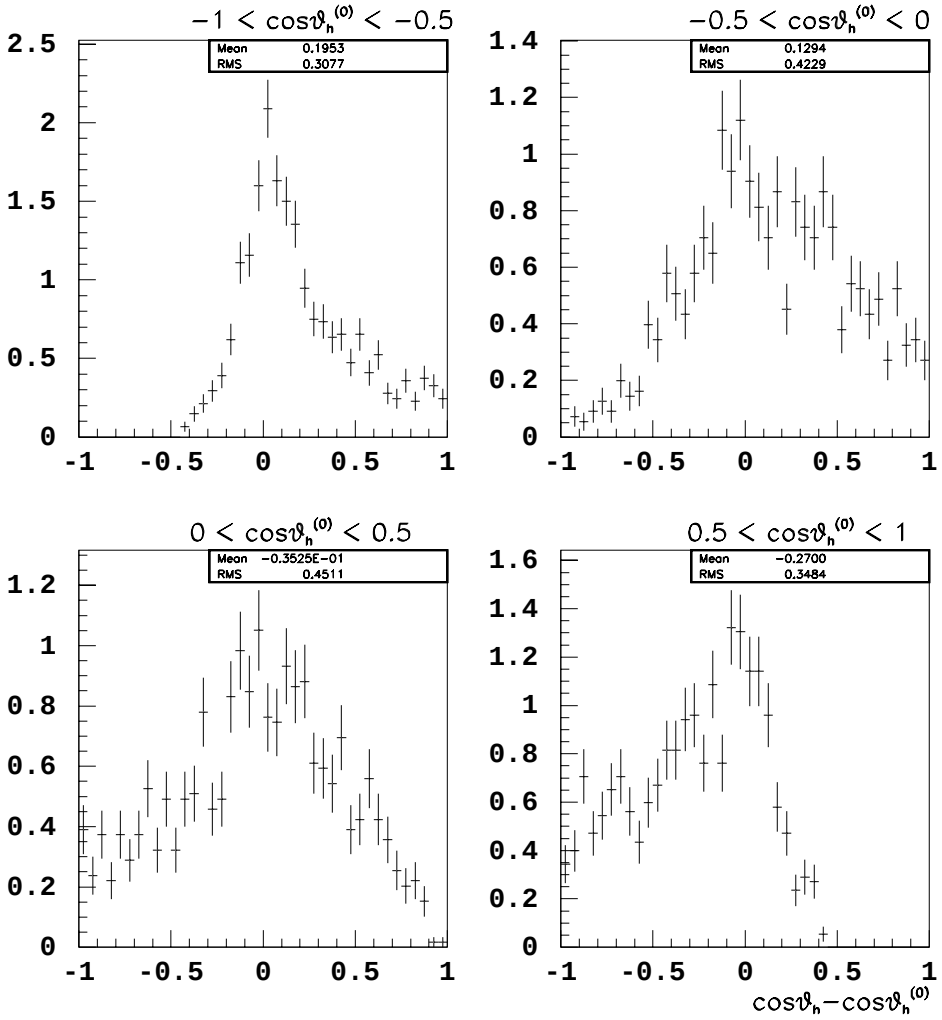

Figure 5.15: Smearing function of the polarimeter polar angle for $\pi 2\pi^0$ channels mis–identified as ρ, in four coarse bins of $\cos\theta_h^{(0)}$.

5.6 Likelihood function summary

Every event identified within one of the decay categories considered is used to provide a likelihood for observing that event as a function of the anomalous coupling strengths. The effects of instrumental resolution on the observed hemisphere parameters (W,$\cos\theta_h$,ϕ_h) and contamination from all known background sources are

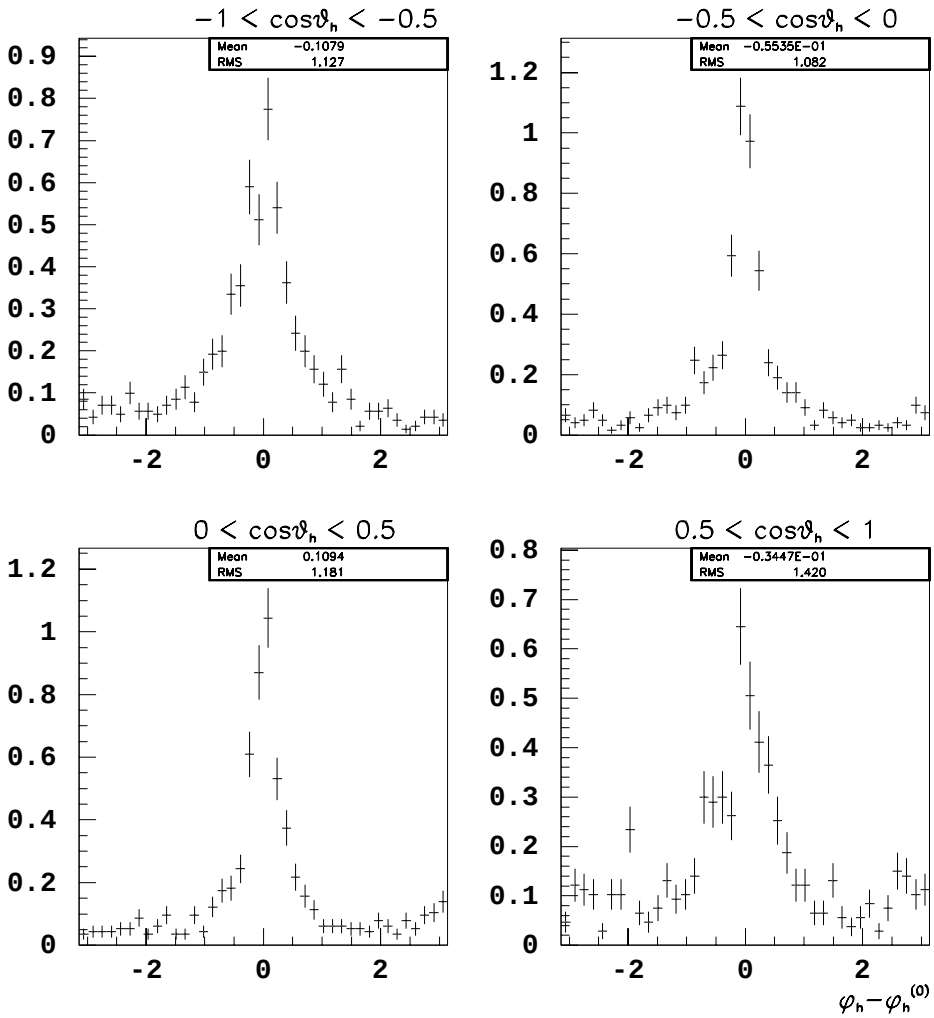

Figure 5.16: Smearing function of the polarimeter azimuthal angle for ρ channels mis–identified as $\pi 2\pi^0$.

incorporated into the effective $\tilde{H}^{\mu}(W, \cos\theta_h, \phi_h)$ functions, which are computed for each identified hemisphere before the likelihood fit is performed. These effective $\tilde{H}$ functions are the weighted sum of the individual $\tilde{H}$ for each physics process expected to be present in a given identified channel, as predicted by the Monte Carlo simulation.

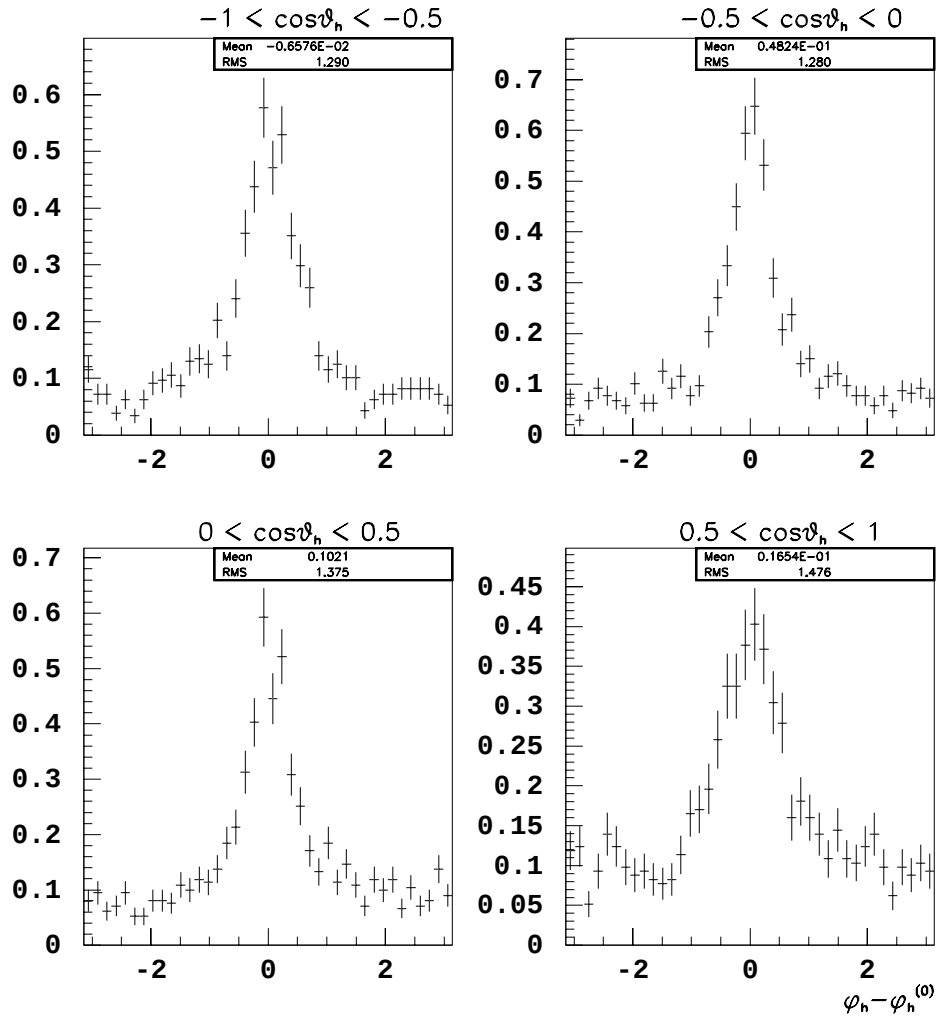

Figure 5.17: Smearing function of the polarimeter azimuthal angle for $\pi 2\pi^0$ channels mis–identified as ρ.

Each identified $\tau^+\tau^-$ in the topology (ij) then contributes a likelihood given by

$$L_{ij} = \bar{R}_{\mu\nu}(\mu_\tau, d_\tau|\Omega)\tilde{H}_i^\mu(W_1, \cos\theta_{h_1}, \phi_{h_1})\tilde{H}_j^\nu(W_2, \cos\theta_{h_2}, \phi_{h_2})\,, \tag{5.11}$$

such that the total likelihood function given by

$$F(\mu_\tau, d_\tau) \equiv -2 \sum_{events} logL_{ij} \tag{5.12}$$

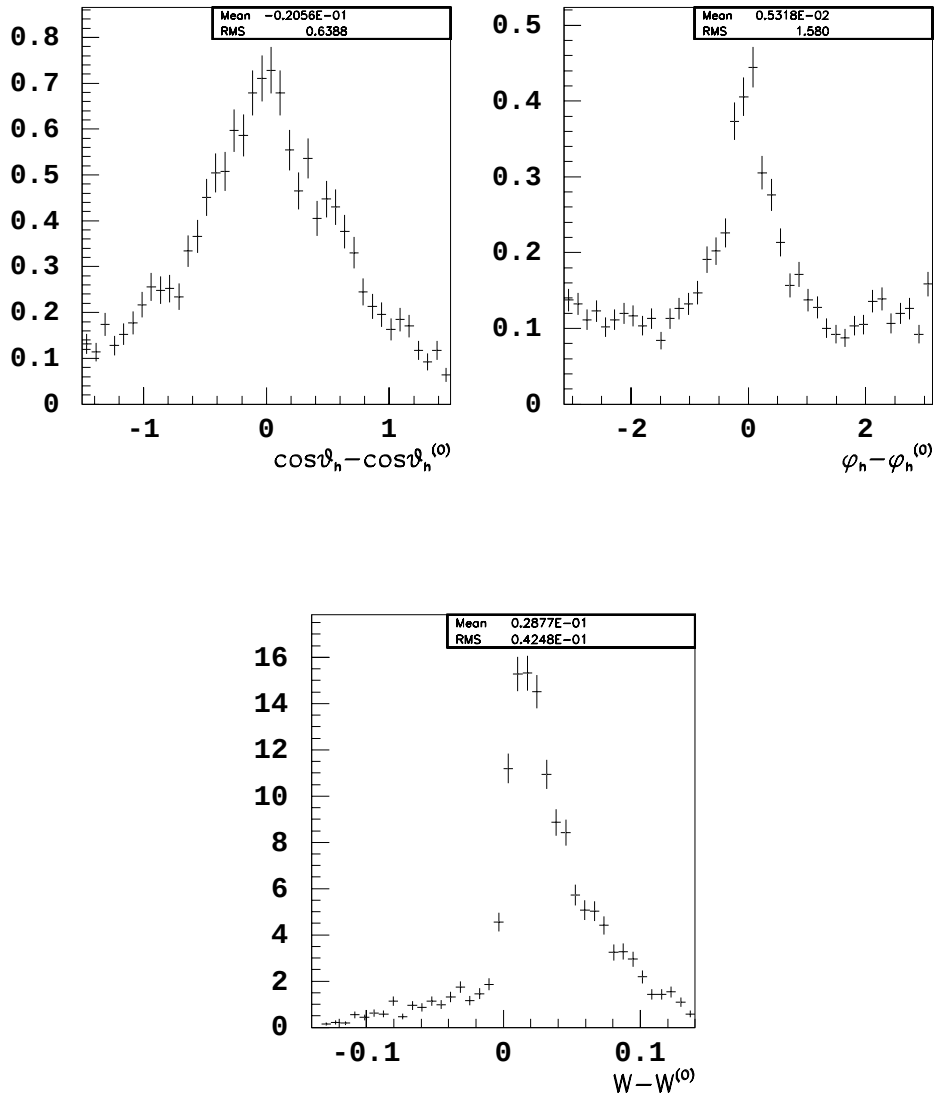

Figure 5.18: $\int D_{other\,\rho}(\cos\theta_h - \cos\theta_h^{(0)}, \cos\theta_h^{(0)}) d\cos\theta_h^{(0)}$ and $D_{other\,\rho}(\phi_h - \phi_h^{(0)})$ (top, left and right) and $\int D_{other\,\rho}(W - W^{(0)}, W^{(0)}) dW^{(0)}$ in the bottom–middle.

can be minimized to find the most likely value of the anomalous dipole coupling parameters. The actual fit results and a discussion of the interpretation of the errors on the fit values will be covered in the next chapter.

Chapter 6

Systematic errors and results

In this chapter, we first test the fitting formula with a *calibration procedure*. Afterwards, the results on the data and some cross checks are presented. Finally, we estimate the most relevant systematic errors and compare with the measurements of other experiments.

6.1 Calibration curves

It is desirable to check the performance of the fitting formula developed in the previous chapter, in an appropriate region of the anomalous couplings around the SM prediction (which is zero except for small radiative correction effects, below our sensitivity), and also taking into account our expected experimental uncertainty. For this purpose, we make use of the SCOT Monte Carlo [39], with a simple radiator function to include the Initial State Radiation [40], and interfaced with the full detector simulation. For every anomalous coupling, we have generated five sets of tau Monte Carlo samples at different values of each coupling. Each set has a size typically equal to that of the tau data sample and branching ratios as in the PDG [23].

Detector effects and background may not be fully simulated in the fitting formula, and this may cause a disagreement between the fitted anomalous couplings and those of the generation. The more relevant background is the contamination of $\pi 2\pi^0$ into ρ and the contamination of ρ into π, as shown in figs. 5.10– 5.12. Since the analytical expressions of the polarimeters differ for each decay topology (see appendix B), an incorrect channel assignment will translate in a dilution of the

underlying tau spin structure; and therefore, in a dilution of the event observables for measuring the weak dipole moments. This all is what we explore below.

For every channel and every anomalous coupling, we have plotted the fitted versus the generated values which, in principle, should lie on a straight line, $y = ax$, intersecting the origin. Any deviation of the a parameters from 1 is an indication of a bias introduced by the fitting formula due to the incorrect modeling of the detector and background effects.

The results of the straight line fits for every channel and every anomalous coupling are shown in table 6.1. For the π–π channel we also present the corresponding curves in fig. 6.1.

The slope is not always compatible with 1, as one would expect if the detector effects and the background were correctly modeled in the formula. For the $\Im(d_\tau)$ parameter in the π–π channel , the deviation of the slope from 1 is very significant. This has been understood as badly reconstructed events (i.e. background), which distort the results. The introduction of the D_{ij} functions is not sufficient to recover the proper values. However, the curves are in most cases good straight lines, as shown by the χ^2 of the fit.

Since we are dealing with a multidimensional fit, the correct description of all the detector effects and background is very difficult. Such effects and processes introduce some correlations between observables which are very difficult to take into account. Therefore, the values obtained with the fit explained in the previous chapter are corrected by the *calibration curves* of table 6.1.

6.2 Likelihood results

As we want to correct the fitted results for every channel and anomalous coupling independently, we need the results for each topology. A four parameter fit is carried out for each final state topology. Therefore, each fit provides four values with certain individual correlation between them, which are found to be very small (typically $\approx 10\%$).

We then obtain a set of measurements $\{\vec{x}_{\pi\pi}, \vec{x}_{\pi\rho}, \cdots\}$, with $\vec{x} = (x_1, x_2, x_3, x_4)$ the four anomalous couplings (the subindex ij of $\vec{x}_{ij}$ stands for the decay topology). From the minimisation, there is some small statistical correlation between the x_l

Channel	$\Re(\mu_\tau)$		$\Im(\mu_\tau)$	
	a	χ^2/ndf	a	χ^2/ndf
π–π	0.79 ± 0.12	$4.63/4$	0.85 ± 0.13	$7.27/4$
π–ρ	0.931 ± 0.055	$9.23/4$	0.649 ± 0.069	$3.99/4$
π–$\pi 2\pi^0$	1.23 ± 0.11	$7.91/4$	0.99 ± 0.13	$1.54/4$
π–3π	1.11 ± 0.11	$3.17/4$	0.91 ± 0.14	$0.14/4$
ρ–ρ	0.937 ± 0.056	$1.54/4$	0.609 ± 0.074	$1.11/4$
ρ–$\pi 2\pi^0$	1.022 ± 0.072	$6.11/4$	0.768 ± 0.099	$5.55/4$
ρ–3π	0.911 ± 0.072	$1.80/4$	0.570 ± 0.095	$0.87/4$
$\pi 2\pi^0$–$\pi 2\pi^0$	1.09 ± 0.19	$0.79/4$	0.70 ± 0.25	$3.70/4$
$\pi 2\pi^0$–3π	1.07 ± 0.13	$1.55/4$	0.57 ± 0.18	$0.34/4$
3π–3π	0.95 ± 0.19	$1.42/4$	0.48 ± 0.27	$1.92/4$
Channel	$\Re(d_\tau)$		$\Im(d_\tau)$	
	a	χ^2/ndf	a	χ^2/ndf
π–π	0.810 ± 0.082	$1.65/4$	0.588 ± 0.096	$2.14/4$
π–ρ	1.078 ± 0.056	$5.03/4$	1.022 ± 0.070	$1.12/4$
π–$\pi 2\pi^0$	1.14 ± 0.11	$3.30/4$	0.79 ± 0.14	$2.49/4$
π–3π	1.22 ± 0.11	$4.08/4$	1.19 ± 0.14	$1.35/4$
ρ–ρ	1.064 ± 0.060	$1.53/4$	0.794 ± 0.076	$1.59/4$
ρ–$\pi 2\pi^0$	1.009 ± 0.077	$2.28/4$	0.89 ± 0.10	$2.62/4$
ρ–3π	0.889 ± 0.072	$2.42/4$	0.612 ± 0.095	$1.51/4$
$\pi 2\pi^0$–$\pi 2\pi^0$	0.96 ± 0.20	$6.63/4$	0.85 ± 0.25	$2.27/4$
$\pi 2\pi^0$–3π	0.90 ± 0.13	$0.62/4$	0.70 ± 0.18	$2.74/4$
3π–3π	0.92 ± 0.19	$2.34/4$	0.69 ± 0.24	$2.09/4$

Table 6.1: Results of the fit of the calibration curves for the magnetic moment (top) and for the electric moment(bottom), for each of the decay topologies. We also give the value of the slope from the fit, a, and the χ^2/ndf.

($l = 1, \cdots, 4$) of a given $\vec{x}_{ij}$, but the correlation between the x_l of different decay topologies is zero.

The set of measurements $\{\vec{x}_{\pi\pi}, \vec{x}_{\pi\rho}, \cdots\}$ with only their statistical errors are presented in figs. 6.2 and 6.3. Each figure gives the results on two anomalous couplings for the various channels. At this stage, all the results are compatible with the SM prediction. The statistical errors vary from $\approx 0.8 \times 10^{-3}$ for the measurement of $\Re(\mu_\tau)$ with the $\rho\rho$ channel to $\approx 4.3 \times 10^{-3}$ for the measurement of $\Im(\mu_\tau)$ with the $\pi 2\pi^0$–$\pi 2\pi^0$ channel.

Once the $\{\vec{x}_{\pi\pi}, \vec{x}_{\pi\rho}, \cdots\}$ are obtained, for every coupling and every topology, we

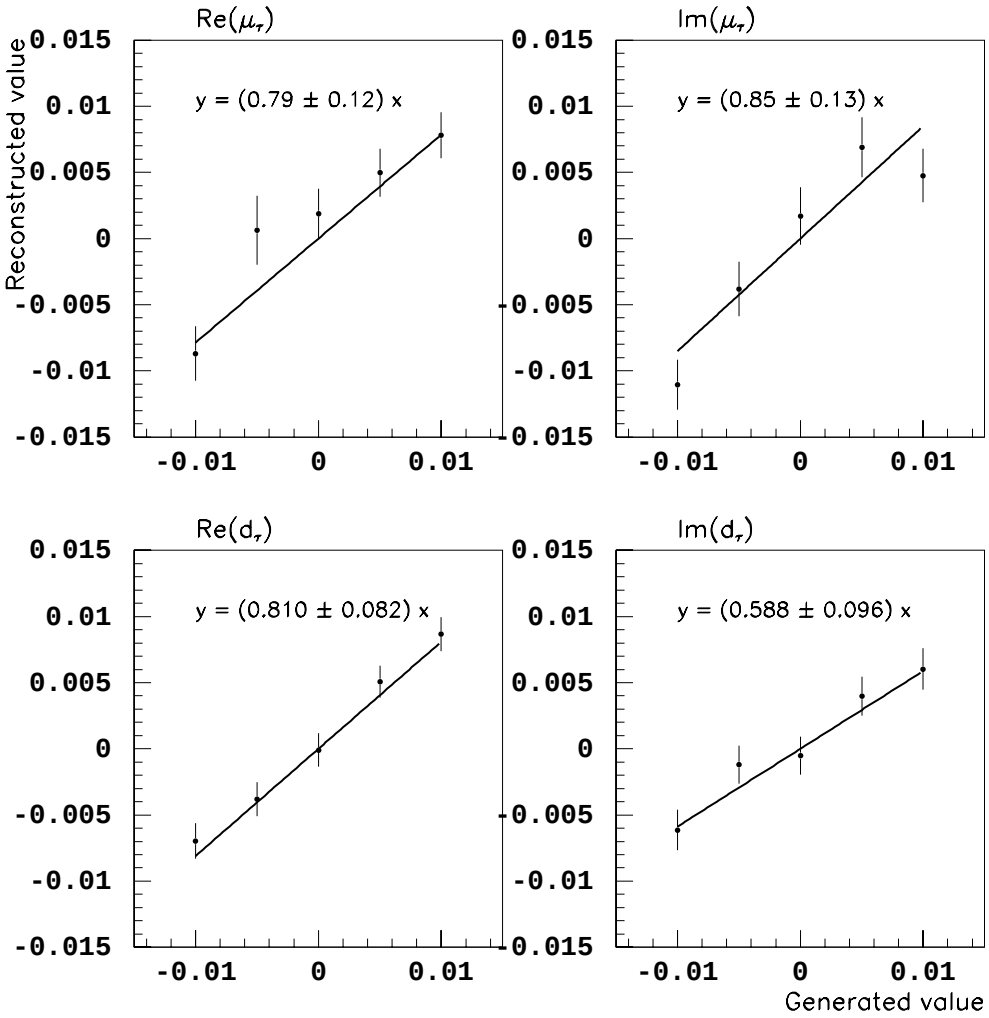

Figure 6.1: Calibration plots for the π–π channel, for $\Re(\mu_\tau)$ and $\Im(\mu_\tau)$ (top–left and top–right); and for $\Re(d_\tau)$ and $\Im(d_\tau)$ (bottom–left and bottom–right). The reconstructed values are plotted versus those of the generation. The fitting curve is $y = ax$ and the result of the fit, a, is shown on each plot.

correct the $\{\vec{x}_{\pi\pi}, \vec{x}_{\pi\rho}, \cdots\}$ by the set of a parameters of the previous section. We then have a set of $\{\vec{y}_{\pi\pi}, \vec{y}_{\pi\rho}, \cdots\}$ measurements, where each y is related with the previous x by $y = x/a$, using the a values of table 6.1, which are different for every anomalous coupling and every decay topology.

Finally, we would like to obtain a vector $\vec{\alpha} = (\alpha_1, \alpha_2, \alpha_3, \alpha_4)$ with the final mea-

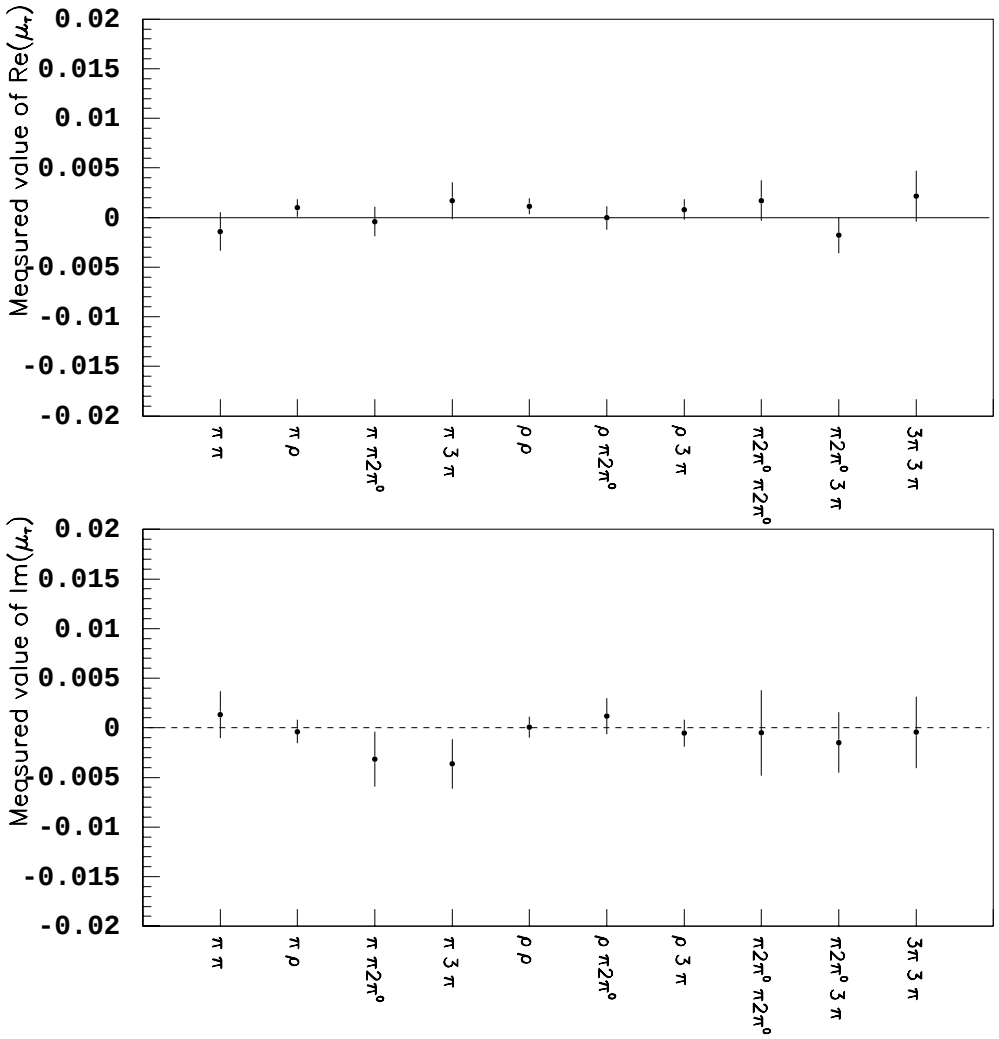

Figure 6.2: Results on the $\Re(\mu_\tau)$ (top), and on the $\Im(\mu_\tau)$ (bottom), versus the various decay topologies.

surements of the anomalous couplings from all the data sample. For this purpose, we minimize the following χ^2:

$$\chi^2 = P\left(V^{-1}\right)P^T \text{ with } P = \begin{pmatrix} \vec{\alpha} - \vec{y}_{\pi\pi} \\ \vec{\alpha} - \vec{y}_{\pi\rho} \\ . \\ . \\ . \end{pmatrix}, \tag{6.1}$$

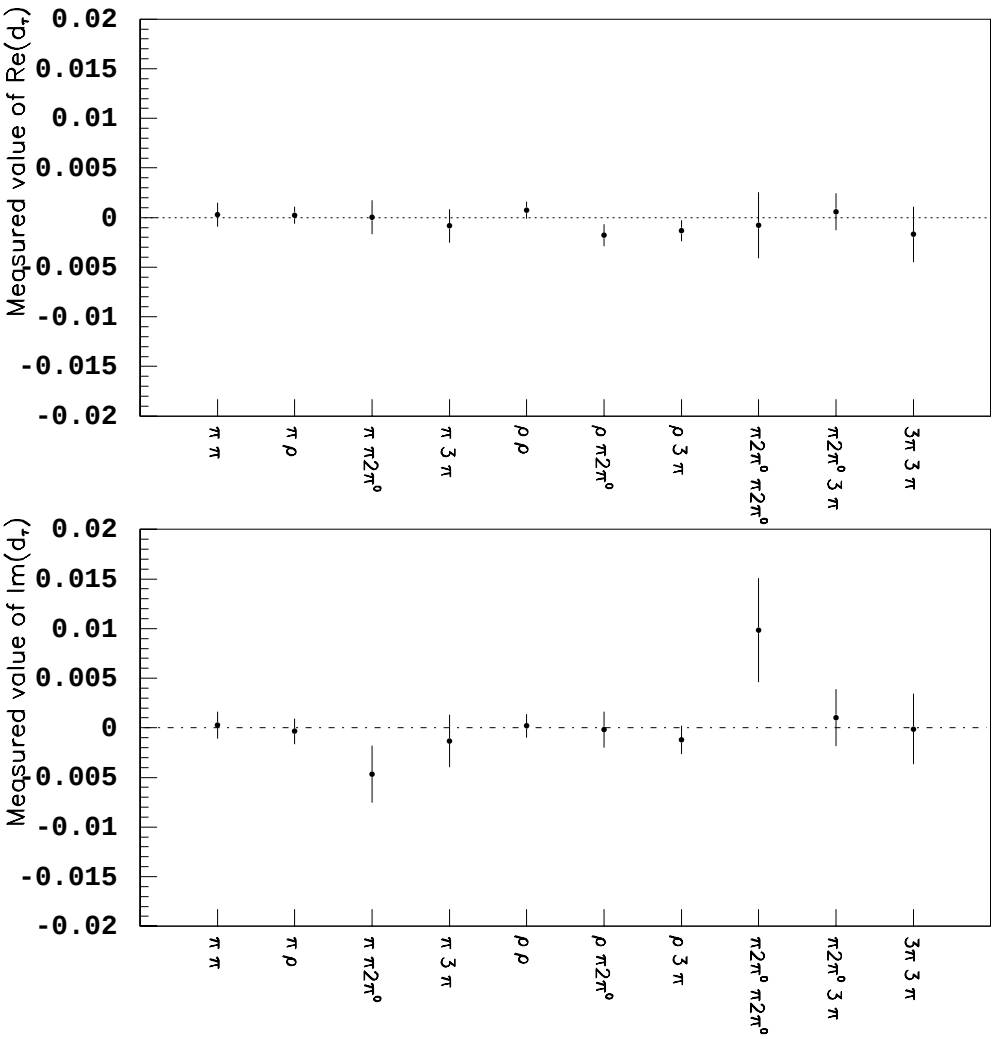

Figure 6.3: Results on the $\Re(d_\tau)$ (top), and on the $\Im(d_\tau)$ (bottom), versus the various decay topologies. The weak electric dipole moment is assumed dimensionless in these figures.

where V is the covariance matrix of the $\{\vec{y}_{\pi\pi}, \vec{y}_{\pi\rho}, \cdots\}$, obtained from the 4 parameter fits performed before. As pointed out already, the only elements with statistical correlation are those belonging to the same topology. Therefore, this covariance matrix is a 40×40 squared matrix, which can be expressed as $(4 \times 4) \times 10 \times 10$, since the non–zero elements are 4×4 squared matrix placed in the diagonal.

The combined results from the minimisation of the χ^2 are presented in table 6.2,

and the individual correlation between the fit parameters in table 6.3.

The errors have decreased considerably from the combination, as it was obviously expected, but the relevant point is that we get very competitive results comparing with the measurements of other experiments. This will be fully covered in the last section of this chapter. The individual correlations between parameters are quite small. Thus, our numbers would not modify substantially if we had obtained them from 1 parameter fits. However, we have preferred to perform 4 parameter fits because the small correlations are taken into account and also because the CPU consumption is not very high.

We could also wonder about the impact of the individual corrections, i.e. those introduced by the a slopes, on the final numbers. To see this effect, we have just minimized the χ^2 of eq. 6.1 replacing the $\{\vec{y}_{\pi\pi}, \vec{y}_{\pi\rho}, \cdots\}$ by the uncorrected $\{\vec{x}_{\pi\pi}, \vec{x}_{\pi\rho}, \cdots\}$. The results are shown in table 6.4. As expected, the effect is more important on ($\Re(d_\tau)$, $\Im(d_\tau)$) than in ($\Re(\mu_\tau)$, $\Im(\mu_\tau)$), because the deviation of the slopes from 1 is more significant for the former parameters.

Parameter	Fit value	σ
$\Re(\mu_\tau)[10^{-3}]$	0.65	0.40
$\Im(\mu_\tau)[10^{-3}]$	-0.68	0.82
$\Re(d_\tau)[10^{-18}\mathrm{e}\cdot\mathrm{cm}]$	-0.89	2.14
$\Im(d_\tau)[10^{-18}\mathrm{e}\cdot\mathrm{cm}]$	1.48	3.77

Table 6.2: Fit values for the weak anomalous dipole moments and 1 σ statistical error, from the 90-95 LEP data sample.

	$\Re(\mu_\tau)$	$\Im(\mu_\tau)$	$\Re(d_\tau)$	$\Im(d_\tau)$	Global
$\Re(\mu_\tau)$	1.0	-0.011	0.049	0.062	0.080
$\Im(\mu_\tau)$		1.0	-0.084	0.062	0.105
$\Re(d_\tau)$			1.0	-0.011	0.098
$\Im(d_\tau)$				1.0	0.088

Table 6.3: Correlation matrix between the fitted parameters.

Parameter	Fit value	σ
$\Re(\mu_\tau)[10^{-3}]$	0.67	0.39
$\Im(\mu_\tau)[10^{-3}]$	-0.43	0.55
$\Re(d_\tau)[10^{-18}\mathrm{e}\cdot\mathrm{cm}]$	-1.10	2.17
$\Im(d_\tau)[10^{-18}\mathrm{e}\cdot\mathrm{cm}]$	-1.04	3.07

Table 6.4: Fit values for the weak anomalous dipole moments and 1 σ statistical error, from the 90-95 LEP data sample, without any correction from the calibration curves. Comparing with table 6.2, we can see that the impact is more significant on the electric terms than in the magnetic terms. This effect is due to the more relevant deviation of the slopes from 1 for the former parameters.

6.3 Systematic checks

Some of the steps taken in the previous section, in particular the calibration curves applied, are corrections for systematic effects arising from the incorrect modeling of background and detector effects in the fitting formula. In addition, we can check that other possible systematic effects are small and do not affect our results.

The fits have been obtained independently for every tau decay channel and the results are consistent, as shown in the figs. 6.2 and 6.3.

Another test comes from the comparison of the data and the Monte Carlo simulation for the event observables. This is shown in fig. 6.4 for the $\cos\theta_h$ of the polarimeter for the four channels considered. Figs. 6.5, 6.6, 6.7 and 6.8 show the comparison of the ϕ_h of the polarimeter in four bins of $\cos\theta_h$ for every channel. Finally, the W variable for the data and the Monte Carlo simulation is presented in fig. 6.9 for the ρ, $\pi 2\pi^0$ and 3π channels.

The angular variables obtained from the data are consistent with those of the simulation. However, the W variable of some channels differs strongly for the data and the Monte Carlo simulation. The most relevant inconsistency on this variable is found for the $\pi 2\pi^0$ channel: the distribution of the W for the data is higher than that of the Monte Carlo simulation by 2 to 4 sigmas in the low W region. However, the sensitivity of the anomalous couplings is stronger for the angular variables. The effect of the W discrepancy will be investigated in the next section.

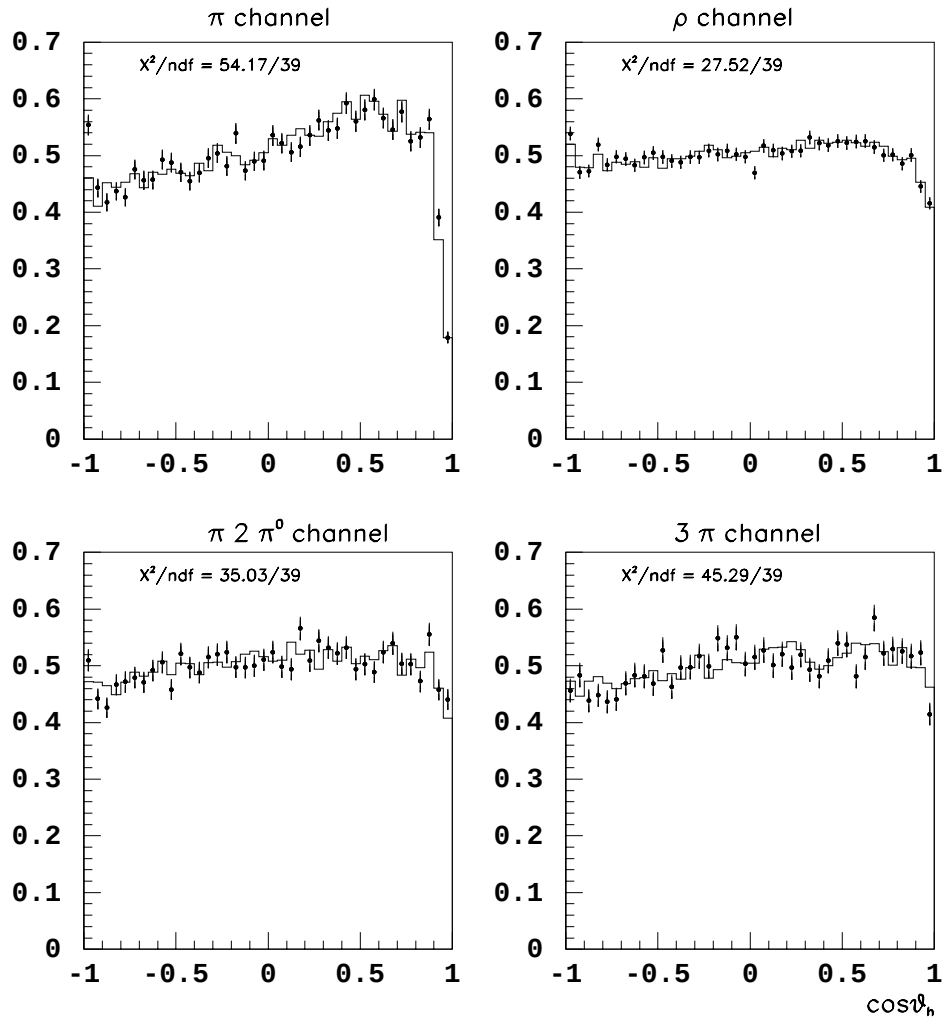

Figure 6.4: Comparison of the $\cos\theta_h$ distribution for the data (points) and the Monte Carlo simulation (lines) for the four channels considered. The areas of all the histograms are normalized to unit, and the χ^2 of the comparison is shown on each plot.

6.4 Systematic uncertainties

The systematic uncertainties coming from different sources have been calculated for every anomalous coupling and decay topology. The estimates are shown in tables 6.5, 6.6, 6.7 and 6.8. The most significant uncertainties are due to ECAL effects, the a_1 dynamic modeling and the W disagreements. This all is covered

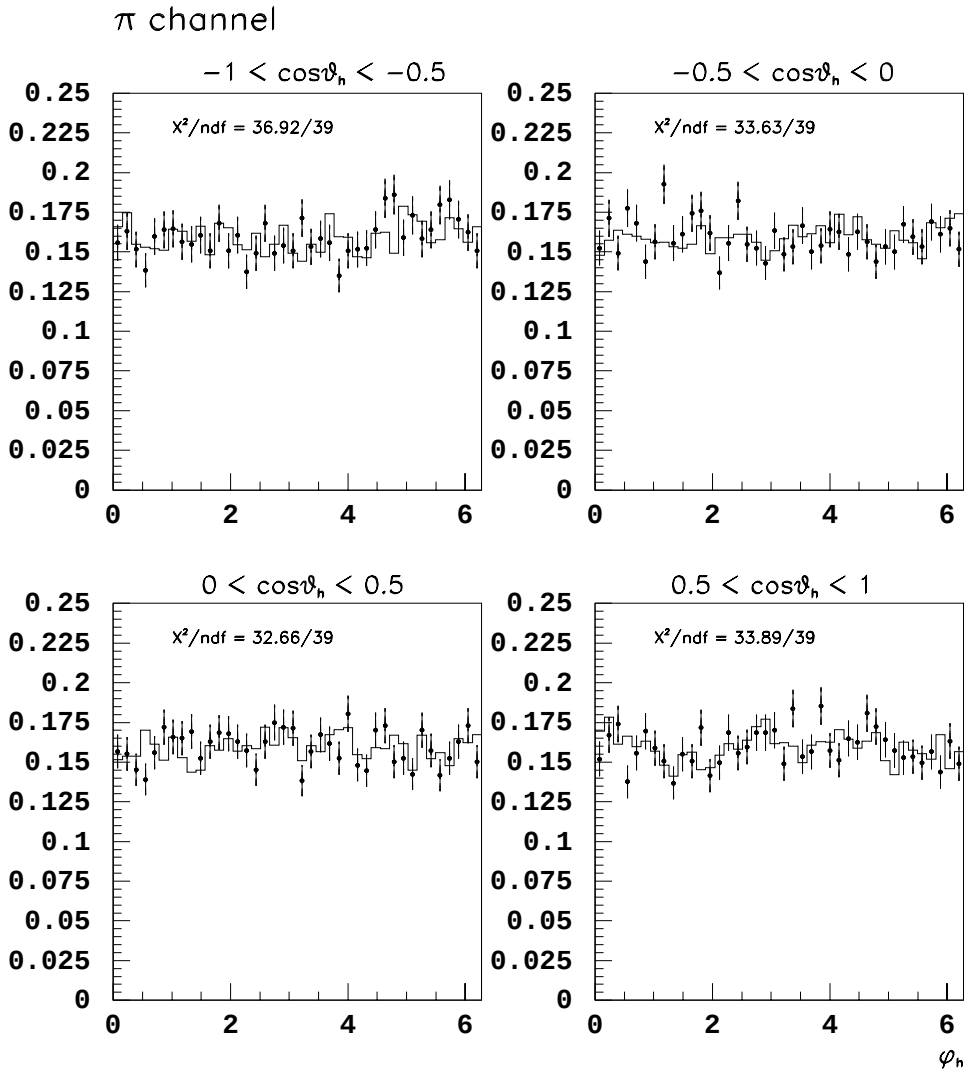

Figure 6.5: Comparison of the ϕ_h distribution for the data (points) and the Monte Carlo simulation (lines) in four bins of $\cos\theta_h$ for the pion channel. The areas of all the histograms are normalized to unit, and the χ^2 of the comparison is shown on each plot.

below.

In all cases, the different sources of systematic effects have been varied up and down within their errors or estimated variation intervals, and the maximum difference in the fitted parameters is quoted as the corresponding systematic error. When various different effects are grouped under the same column, a geometrical

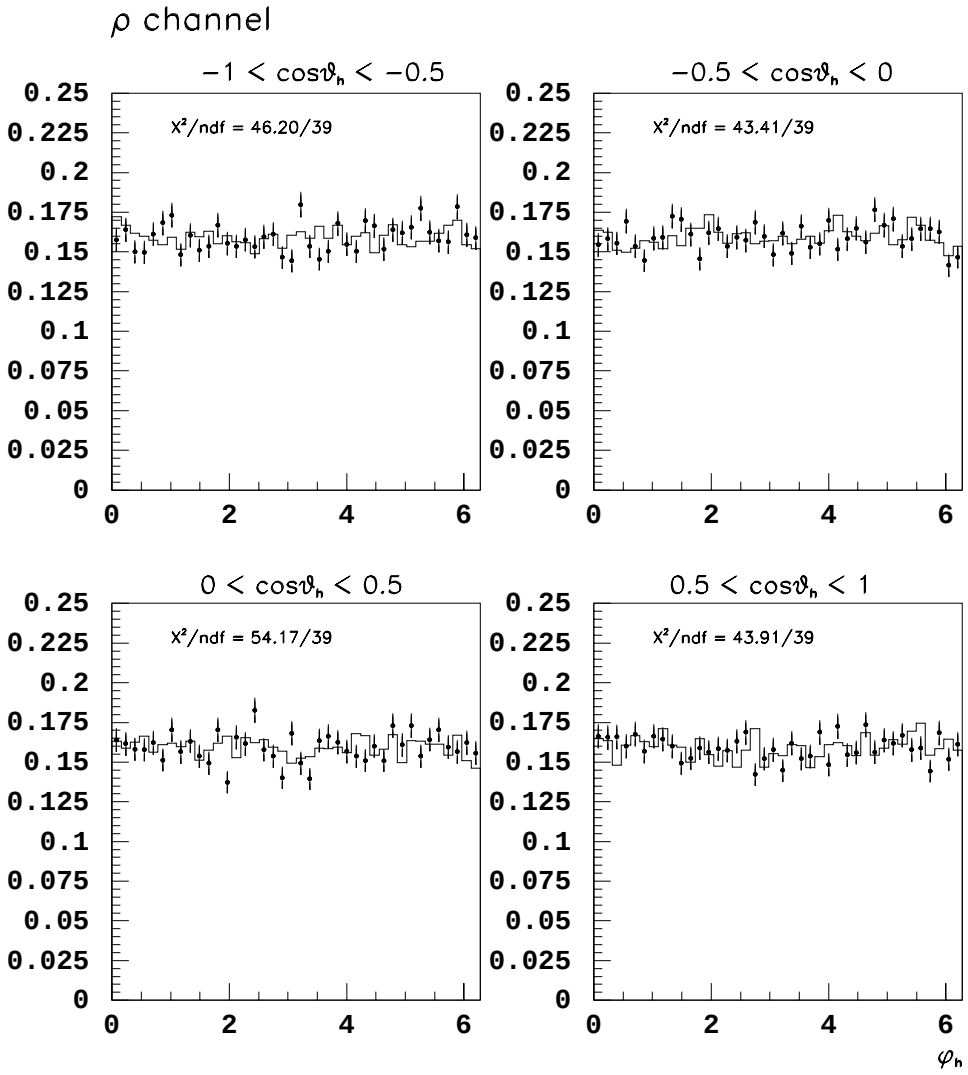

Figure 6.6: Comparison of the ϕ_h distribution for the data (points) and the Monte Carlo simulation (lines) in four bins of $\cos\theta_h$ for the ρ channel. The areas of all the histograms are normalized to unit, and the χ^2 of the comparison is shown on each plot.

mean is applied to the individual errors in order to obtain the number in the column.

In previous tau analysis in ALEPH, the response of the electromagnetic calorimeter ECAL has been observed to introduce relevant systematic effects on the measurement of the energy of events [46]. Here, we explore the error due to the uncertainty in the global scale, and the error due to the mis–intercalibration between modules.

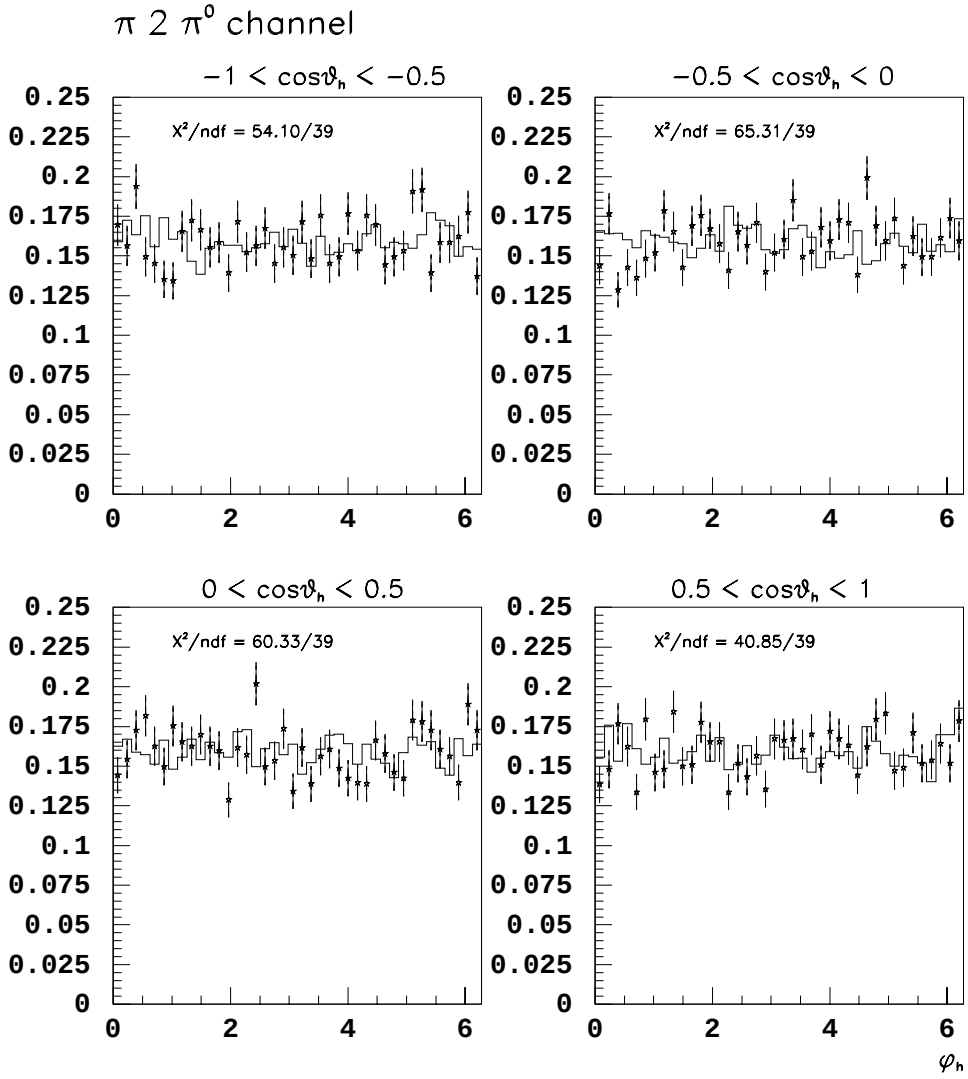

Figure 6.7: Comparison of the ϕ_h distribution for the data (points) and the Monte Carlo simulation (lines) in four bins of $\cos\theta_h$ for the $\pi 2\pi^0$ channel. The areas of all the histograms are normalized to unit, and the χ^2 of the comparison is shown on each plot.

For the total scale, global variations of the ECAL modules by a factor of $\pm$ 0.7% have been considered. The estimate of the systematic error has been obtained, as already said, taking the maximum difference of the fitted parameters. For the intercalibration between modules, a random mis–intercalibration of 0.4% has been applied, obtaining an independent error estimate for this effect. The geometrical

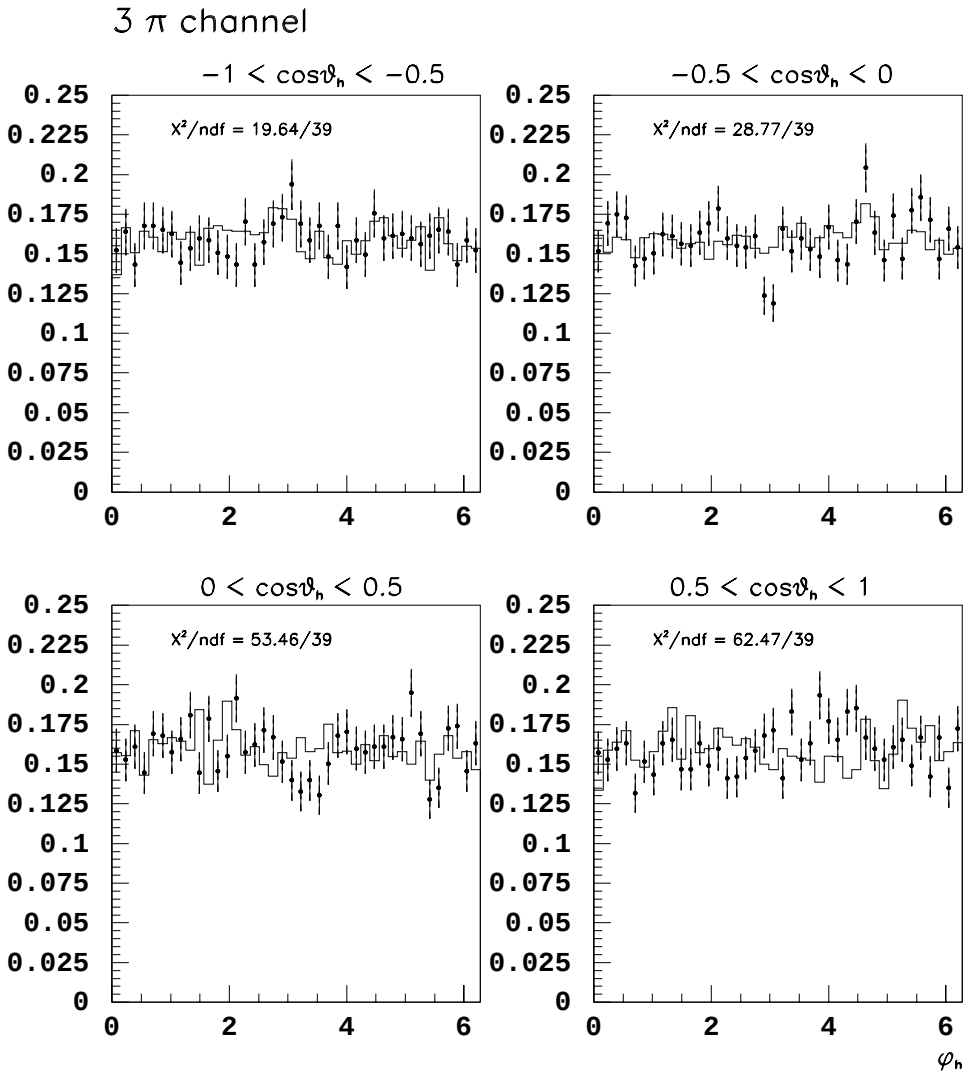

Figure 6.8: Comparison of the ϕ_h distribution for the data (points) and the Monte Carlo simulation (lines) in four bins of $\cos\theta_h$ for the 3π channel. The areas of all the histograms are normalized to unit, and the χ^2 of the comparison is shown on each plot.

average of these two uncertainties is presented under ECAL in the tables mentioned above.

Variations in the τ branching fractions (τ BF in the tables) can also introduce systematic effects. They have been estimated by varying the pion and the electron branching fractions within their errors in the fitting formula. The former is needed

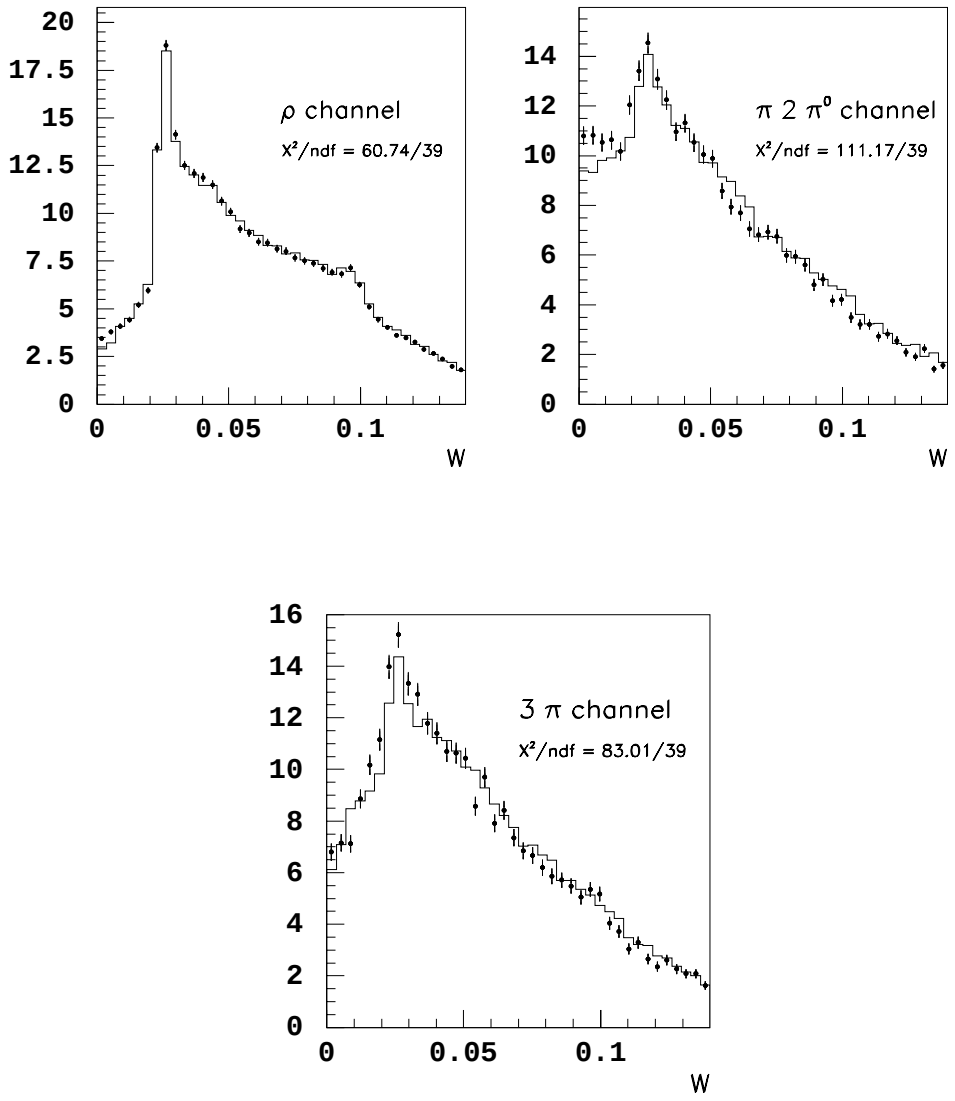

Figure 6.9: Comparison of the W distribution for the data (points) and the Monte Carlo simulation (lines) for the ρ, $\pi 2\pi^0$ and 3π channels. The areas of all the histograms are normalized to unit, and the χ^2 of the comparison is shown on each plot.

to get W of the pion, and the latter is used for normalisation, since in our formula we express the W's in units of Γ_e. These are the two only points in the fitting formula where the branching fraction are used. Other possible effects from this source would appear either in the shape of the resolution functions, the efficiency

functions or in the slope of the calibration curves. These would be "higher order corrections".

The uncertainties under the "Weak par." column are due to variations of the $\sin^2\theta_W$ and M_Z within their experimental errors in the fitting formula. Other weak parameters have negligible effect on the measurements.

The "MC stat." errors are due to the finite Monte Carlo statistic in the determination of the efficiency matrix. Global variations up and down of the mean values of each bin have been performed in order to see the sensitivity to this source of error.

The theoretical model to describe the a_1 dynamic is not perfect. For the measurement of the ALEPH polarisation in the past [47], this correction was evaluated implementing several models in the analysis [48]. For this analysis the implementation of the models is considerably more difficult. To estimate this effect we have done the analysis with three different models: the Kuhn & Santamaria (KS) model [49] (considered in the fitting formula), the Feindt model [50] and the Isgur Morningstar and Reader (simplified) model [51]. The effect of the two latter models in the W and in the third component of the $\vec{h}$ vector were calculated, and the ratio with the corresponding values of the KS model were used to scale the error.

Finally, the disagreement between the data and the Monte Carlo simulation on the W distributions, which was presented in section 6.3, has been quoted as another systematic error. It is certainly the most relevant systematic uncertainty in most of the measurements. To obtain the numbers in this column we have weighted the W observable from the data by the quotient MC/data of the plots of fig. 6.9.

Finally, the total systematic uncertainty is expressed for every parameter and every channel, obtained as the geometrical average of the different sources of systematic errors.

6.5 Final results and comparison with other experiments

To obtain the final results, we include in the diagonal of eq. 6.1 the total error and perform the χ^2 minimisation. This total error is the geometrical mean of the

	ECAL	τBF	Weak par.	MC stat.	a_1 dyn.	W dis.	TOTAL
π–π	5.70	4.65	0.08	5.52	0.	0.	9.20
π–ρ	1.81	2.18	0.11	2.47	0.	2.41	4.47
π–$\pi 2\pi^0$	5.86	1.50	0.06	1.64	0.47	0.14	6.29
π–3π	0.55	1.97	0.15	2.17	1.34	2.96	4.41
ρ–ρ	1.28	1.29	0.10	1.39	0.	0.71	2.40
ρ–$\pi 2\pi^0$	1.98	1.00	0.06	1.19	1.86	1.02	3.29
ρ–3π	4.10	0.84	0.07	0.97	0.54	1.27	4.51
$\pi 2\pi^0$–$\pi 2\pi^0$	11.28	0.21	0.13	0.38	11.02	5.87	16.83
$\pi 2\pi^0$–3π	3.36	0.32	0.02	0.40	2.60	1.07	4.41
3π–3π	6.09	0.75	0.24	0.79	4.79	0.04	7.83

Table 6.5: Systematic uncertainties on $\Re(\mu_\tau)$ for the different channels, and on the last column the total systematic uncertainty for each final state topology. The errors are expressed in units of 10^{-4}.

	ECAL	τBF	Weak par.	MC stat.	a_1 dyn.	W dis.	TOTAL
π–π	2.14	0.65	0.09	0.74	0.	0.	2.36
π–ρ	1.61	0.16	0.03	0.28	0.	1.29	2.09
π–$\pi 2\pi^0$	8.35	0.61	0.32	0.66	7.25	5.43	12.36
π–3π	3.22	0.74	0.21	0.96	6.91	1.26	7.83
ρ–ρ	0.97	0.36	0.05	0.40	0.	0.19	1.12
ρ–$\pi 2\pi^0$	3.79	0.06	0.04	0.20	1.40	2.81	4.92
ρ–3π	0.70	0.08	0.05	0.08	1.22	4.65	4.86
$\pi 2\pi^0$–$\pi 2\pi^0$	8.69	0.22	0.34	0.30	4.28	14.62	17.54
$\pi 2\pi^0$–3π	7.34	0.21	0.16	0.20	8.96	6.50	13.29
3π–3π	2.05	0.72	0.17	1.04	5.88	1.30	6.49

Table 6.6: Systematic uncertainties on the $\Im(\mu_\tau)$ for the different channels, and on the last column the total systematic uncertainty for each final state topology. The errors are expressed in units of 10^{-4}.

previous statistical error and the total systematic uncertainty.

Therefore, the minimisation of the updated eq. 6.1 now provides the measurement of the weak anomalous couplings with their total errors. The results of the fit are expressed in table 6.9, where the total error from this minimisation is denoted as σ, the statistical error as σ_{stat} and the systematic error as σ_{sys}. The statistical error is the value obtained before and the systematic uncertainty σ_{sys} is the geometrical